2018

Development and Modeling of a Biomimetic Punting Unmanned Underwater Vehicle

Matthew Perkins
University of Rhode Island, protoserv@gmail.com

DEVELOPMENT AND MODELING OF A BIOMIMETIC PUNTING UNMANNED UNDERWATER VEHICLE

BY

MATTHEW PERKINS

A THESIS SUBMITTED IN PARTIAL FULFILLMENT OF THE REQUIREMENTS FOR THE DEGREE OF

MASTER OF SCIENCE

IN

OCEAN ENGINEERING

UNIVERSITY OF RHODE ISLAND

2018

MASTER OF SCIENCE THESIS

OF

MATTHEW PERKINS

APPROVED:

Thesis Committee:

Major Professor Stephen C. Licht

Jason M. Dahl

Richard J. Vaccaro

Nasser H. Zawia

DEAN OF THE GRADUATE SCHOOL

UNIVERSITY OF RHODE ISLAND

2018

ABSTRACT

This thesis details the development of a novel propulsion system for unmanned underwater vehicles (UUV's) inspired by the punting locomotion of the 'Little Skate'. The hybrid legged, gliding and punting gait is a potential enabling technology for UUV access to complex littoral environments. Design, development and initial trials with the prototype vehicle are presented. A combination of video motion capture and on-board inertial sensing is validated and used for preliminary analysis of a limited set of punting gaits. The results indicate the importance of matching vehicle morphology and kinematics to achieve effective locomotion and that the prototype is viable to be used as a validation tool for a general punting dynamic model that is in development. A practical method for modeling the vehicle is also presented with results comparing the model to experimental trials.

ACKNOWLEDGMENTS

My work throughout this research has challenged me in many ways that I never expected, but I am truly grateful for opportunity and experience. I would first like to thank Professor Stephen Licht for his guidance, help,and advice. It was wonderful to study under such an accomplished individual with a world of expertise and knowledge. Thank you for making me part of the R-CUE team and believing in me throughout the entire process. I will build upon what I have learned here for years to come. Second, I would like to acknowledge the efforts of Sam Rauworth, and Jordan Kirby. Without their help, this would not have been possible. Finally I would like to thank my friends and family for the help and support through the rough times.

TABLE OF CONTENTS

Page

CHAPTER 1

Introduction

Unmanned underwater vehicles (UUVs) have a proven track record as reliable, versatile platforms for scientific, commercial, or military applications. Current UUV technology does, however, have its limitations. Conventional UUV's are torpedo shaped bodies, with a propeller and lifting surfaces for control. While effective in calm waters, they do not perform well in areas of more dynamic flow, nor in near bottom or complex environments. Access to these areas is essential for the furthering study of nearshore ocean dynamics, removal of unexploded ordinance and countless other applications. This has led to an increase in biomimetics and bio-inspired engineering in order to develop novel ideas for new generations of UUVs. Fish and their propulsion mechanisms are an active area of study with most of the efforts focused on body-caudal fin (BCF) and median or paired fin (MPF) methods as defined in Sfakiotakis et al. [1999]. Flapping foils in the lab [Tangorra et al., 2006] and in the field, [Tangorra et al., 2006], [Techet, 2007], and [Ade], have been implemented in vehicles using various swimming schemes, such as those akin to the ray [Fish et al., 2011], tuna [Anderson and Chhabra, 2002], or turtle [Licht, 2008].

1.1 Motivation

Complex underwater environments are difficult to navigate through, hindering efforts of robotics to operate in these areas. Over time, aquatic animals have adapted different forms of propulsion to move through these complex undersea environments. Littoral zones, specifically, frequently have strong currents, and obstacles, and their shallow depths limit operations of UUVs in these areas. Researchers in the past have taken inspiration from ocean creatures to design vehicles

better suited for specific environments. Taking motivation from the 'Little Skate', a prototype 'punting' vehicle was designed, developed and tested with the goal of improving access to near bottom and near shore environments. It is hypothesized that this propulsion method will improve the ability of underwater vehicles to move along the sea floor in complex environments in the hopes of aiding in scientific study or military operations.

1.2 Thesis Content

The following chapter, Chapter 2, is a review of literature pertaining to underwater vehicles, the Little Skate, and its mode of locomotion termed 'punting'. The background information is provided to give context the work presented in this paper. Chapter 3 details the development and testing of the mechanical prototype punting vehicle. Chapter 4 provides an introduction to modeling the punting vehicle and results obtained. Chapter 5 provides insight into sources of error and future work. Finally, the conclusions drawn from the present work are stated, followed by the bibliography.

CHAPTER 2

Background

2.1 Bio-Inspired Vehicles

Biomimetics and bio-inspired engineering are fields using the observation of biological subjects such plants or animals to inspire new technological inventions. The variety of underwater vehicles has grown from the work of biomimetics and there are a wide range of autonomous and remotely operated vehicles based on sea life to improve the performance of these vehicles for specific tasks.

Figure 2.1.1: Fish-like Biomimetic Vehicle [Listak et al., 2007]

Listak et al. [2007] developed a bio-inspired fish-like vehicle prototype for environmental monitoring shown in Figure 2.1.1. The 16 kilogram, 1.5 meter long vehicles consists of 3 flippers. One, located at the rear, acts as a rudder and provides the main propulsion, while the other two are used for additional propulsion

and depth control. The vehicle has active buoyancy control, an inertial measurement unit, cameras and sonar, and can be towed using the flippers solely for depth control [Listak et al., 2007]. The vehicle was tested in its towing configuration to analyze its ability to submerge and ascend using its fins. When towed, it was found the vehicle was suitable for near bottom visual inspections in areas of volatile sediments with the ability to submerge and ascend at adequate speeds to follow the irregular bottom.

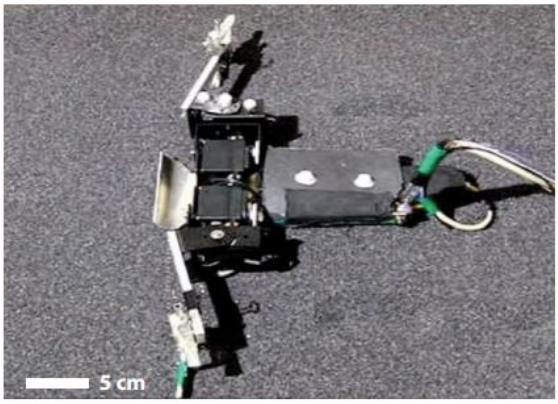

Figure 2.1.2: FlipperBot Biomimetic Vehicle [Mazouchova et al., 2013]

Flipperbot, shown in Figure 2.1.2, is a vehicle developed to study the mechanics of the terrestrial locomotion with flippers. [Mazouchova et al., 2013] The vehicle's design is based on sea turtle hatchlings and their movement through sand. The vehicle is 40cm wide by 19cm long and consists of an aluminum body with four servo motors attached. Two motors lift the arms up and down while the other two move the flippers forward and backward. The servos are used together to create different gaits to propel the vehicle over a sand-like medium. The vehicle was used to gain insight into the principles of flipper-based locomotion on granular media. FlipperBot was tested with two different wrist configurations and various gaits. A free wrist configuration where the flipper that sinks into the sand is allowed to rotate with respect to the arm that drives it was found to to greatly outperform a

fixed wrist that is rigidly attached to the arm. The performance of the vehicle was also sensitive to flipper penetration where a slight decrease in penetration led to a greater decrease in step displacement. This vehicle is not ready to be deployed in open ocean environments but these tests have given insight into amphibious propulsion of marine vehicles.

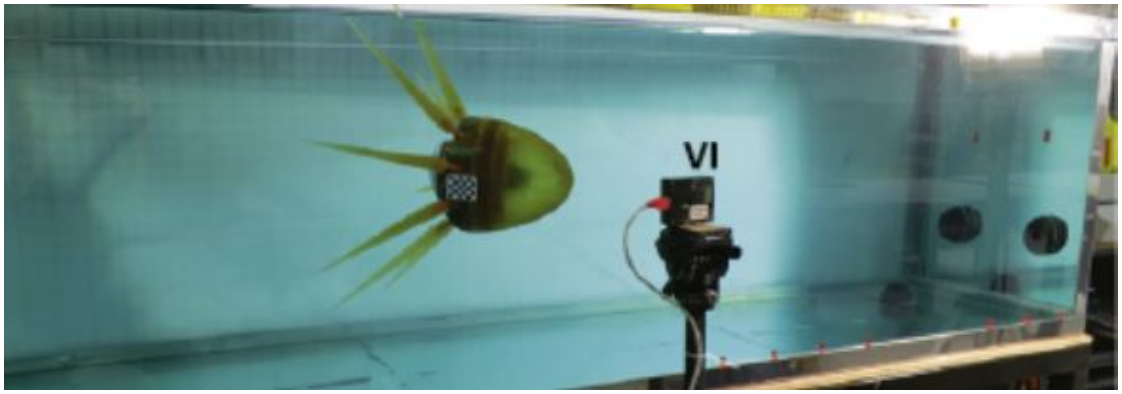

Figure 2.1.3: Octopus inspired vehicle [Sfakiotakis et al., 2015]

The Institute of Computer Science and Foundation for Research and Technology in Heraklion, Greece has developed a multi-functional robot inspired by the octopus. The vehicle body is made of PMC-746 urethane rubber, cast to form interior spaces that hold the electronics and buoyancy elements. 8 legs, each 20cm long and driven by its own waterproof micro-servomotor, are arranged symmetrically about the body. The vehicle propels itself by moving its 8 arms in a synchronous sculling motion with a fast propulsion phase and slow recovery phase, taking advantage of the large inertial forces incurred through large accelerations. The vehicle is able to achieve speeds of 0.26 body lengths per second and can perform turning maneuvers through asymmetric movement of the legs. The vehicle is also able to grasp objects between two of its legs and propel itself forward with the remaining limbs to carry an object through the water. This prototype has great potential for future vehicles that can adapt to a variety of tasks and would

perform well in stealth operations where its biomimetic movement would hide it from investigation.

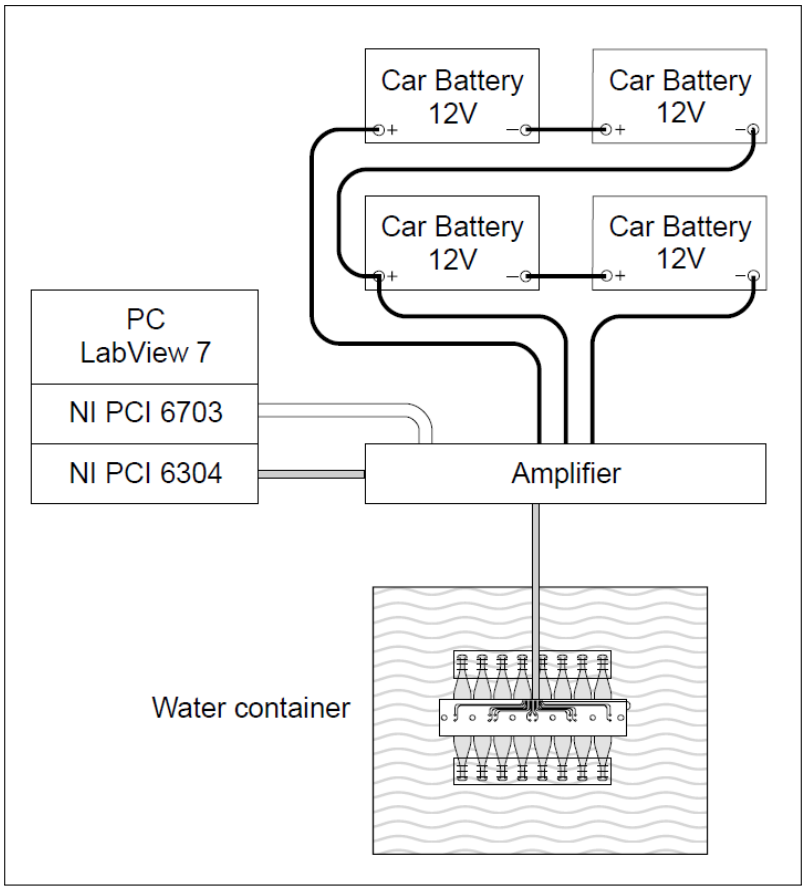

Figure 2.1.4: Experimental setup for ray like biomimetic vehicle. [Punning et al., 2004]

Punning et al. [2004] details the development of a ray like vehicle built using Electroactive polymers (EAPs). EAPs are materials whose shape can be alter by the direct application of an electric field and are used to mimic the behavior of muscles. Punning et al. [2004] uses 16 of these artificial muscles in a vehicle that replicates the rajiform locomotion used by ray and skates. In rajiform swimming, the animals propel themselves by passing waves through their pectoral fins. With 8 of these EAP muscles in each wing, the vehicle was able to propel itself by coordinating the contraction of the muscles to create thrust generating waves in the

latex fins. This vehicle still has offboard computing and power, but the prototype shows the potential of this type of propulsion mechanism.

These vehicles are all examples showing the variety of vehicles that have been biologically inspired and many can provide benefits to a vehicle designed to perform a specific task or operate in a specific environment. The aim of the vehicle in this paper is to operate in the near-bottom or near-shore complex environments such as the surf zone, rivers, or estuaries.

2.2 Crawling Vehicles

There has been active interest in designing vehicles to operate in these complex environments near shore environments, not all of which has centered on biologically inspired work. A large portion of the ROV/AUV market is made up of crawling vehicles. Crawling vehicles are designed with wheels or tracks that can travel along the bottom remaining in contact with the seafloor at all times. These vehicles provide stable platforms that can travel through the surf zone and continue along the sea floor collecting data and performing surveys.

Figure 2.2.1: Modular Amphibious Research Crawler entering the surf. [Wood, 2006]

Wood [2006] at the Florida Institute of Technology(FIT) has developed a crawling ROV specifically designed for scientific studies inside the surf zone. MARC-1 can be controlled from shore or floating platform in depths up to 5 meters and distance from the control station ranging up to 165 meters. The vehicle is equipped with sensors to gather environmental data along the shoreline.

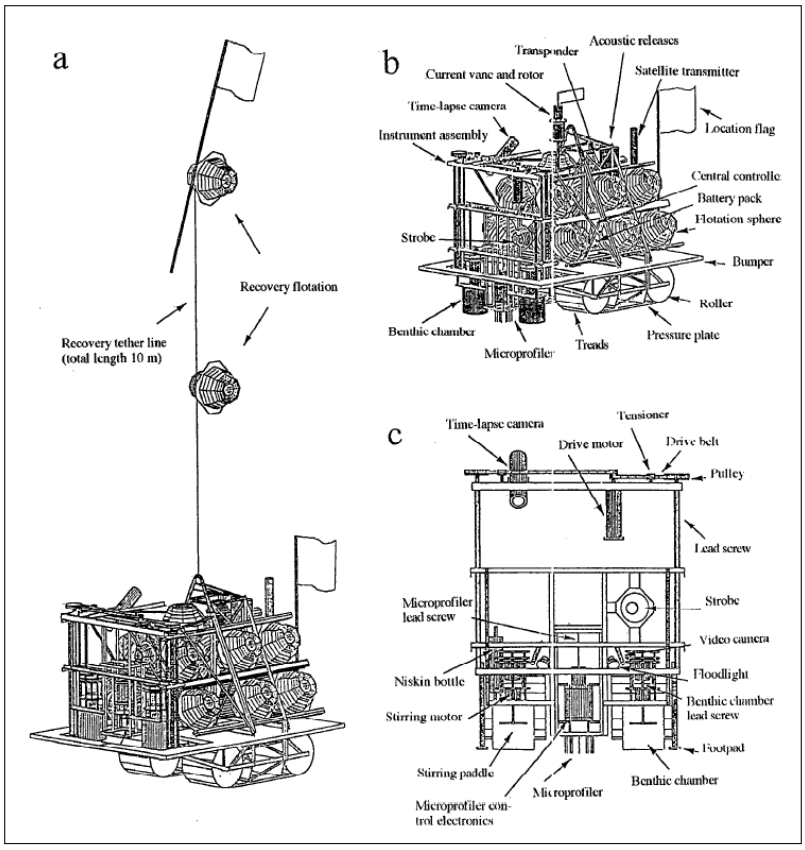

Figure 2.2.2: Layout of the autonomous bottom transecting vehicle developed by the Scripps Institute. [Smith et al., 1997]

Scripps Institute of Oceanography [Smith et al., 1997] has developed a deep-sea bottom crawler that provides a stable platform for data collection to depths of 6,000 meters for up to 6 months. The vehicle can be used for a wide variety of boundary-layer measurements near the sea floor and can collect water samples and oxygen concentrations.

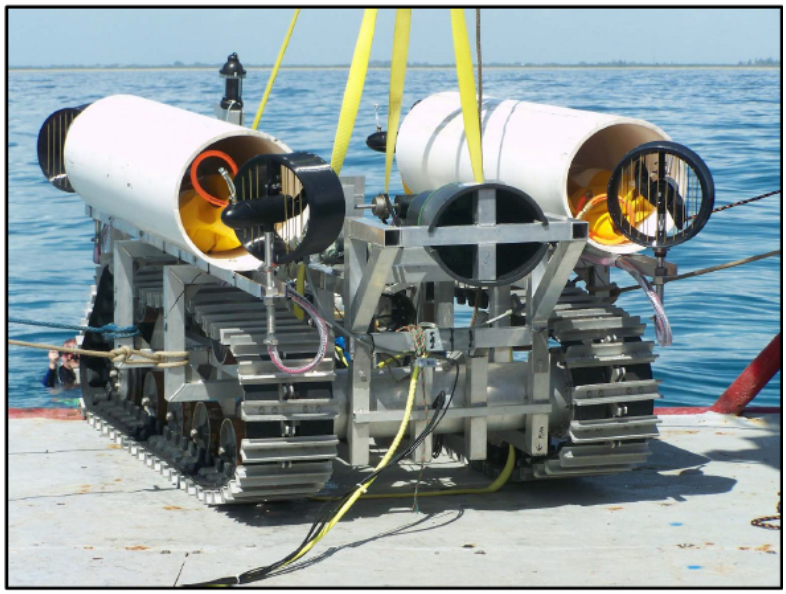

Figure 2.2.3: Hybrid Robot Crawler/Flyer. [Wood et al., 2013]

Wood et al. [2013] at FIT also developed a remotely operated crawler/flyer that moves along the bottom collecting data or investigating areas of interest but also has the ability to inflate additional buoyancy bladders and move through the water column with thrusters. This allows the vehicle to move quickly over adverse terrain and avoid sensitive areas such as reefs without damaging the sea life.

2.3 Underwater Walking Vehicles

Aside from crawlers researchers have also looked toward walking vehicles for access these complex regions.

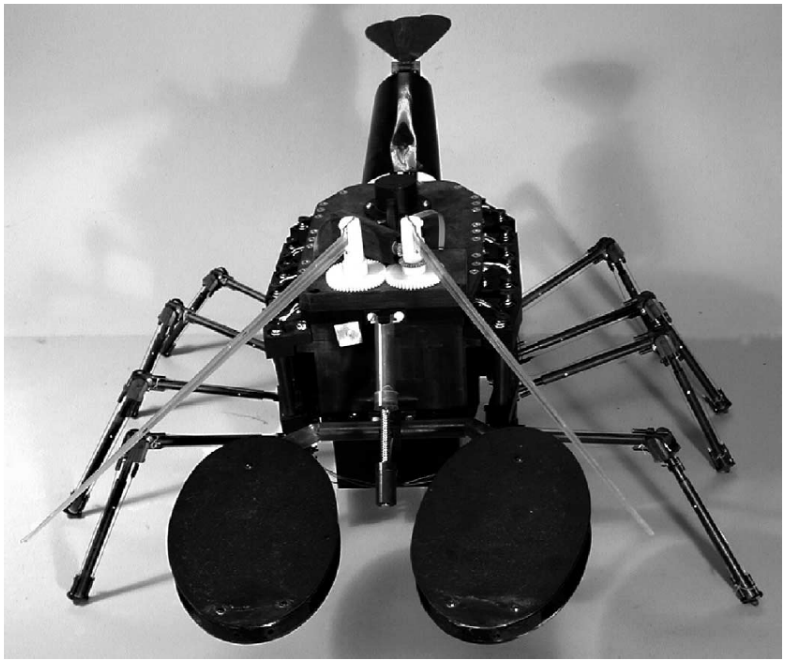

Figure 2.3.1: Biomimetic lobster inspired vehicle. [Ayers, 2004]

Ayers [2004] developed a biomimetic robot based on the lobster that moves with artificial muscle actuators and sensors. The vehicle mimics the movements of the legs of a lobster as well as the tail in order to reduce traction and surge while underwater, advantages commonly found in lobsters.

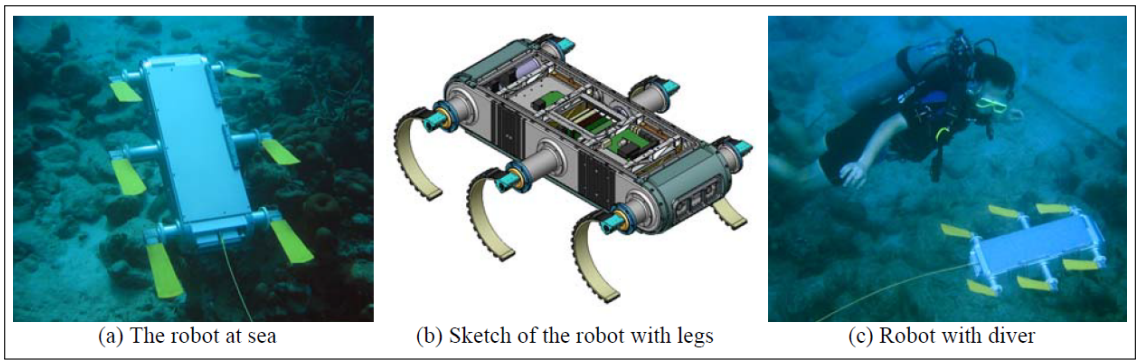

Figure 2.3.2: AQUA: an aquatic walking robot. [Georgiades et al., 2004]

Georgiades et al. [2004] describe an underwater walking robotic system coined AQUA. The vehicle, based on the RHex hexapod robot from Boston Dynamics, is equipped with sensor based navigation and mapping algorithms to allow it to

perform mapping surveys of clear shallow water environments. The six legs allow it to walk along the shore, enter the water and continue traversing the bottom.

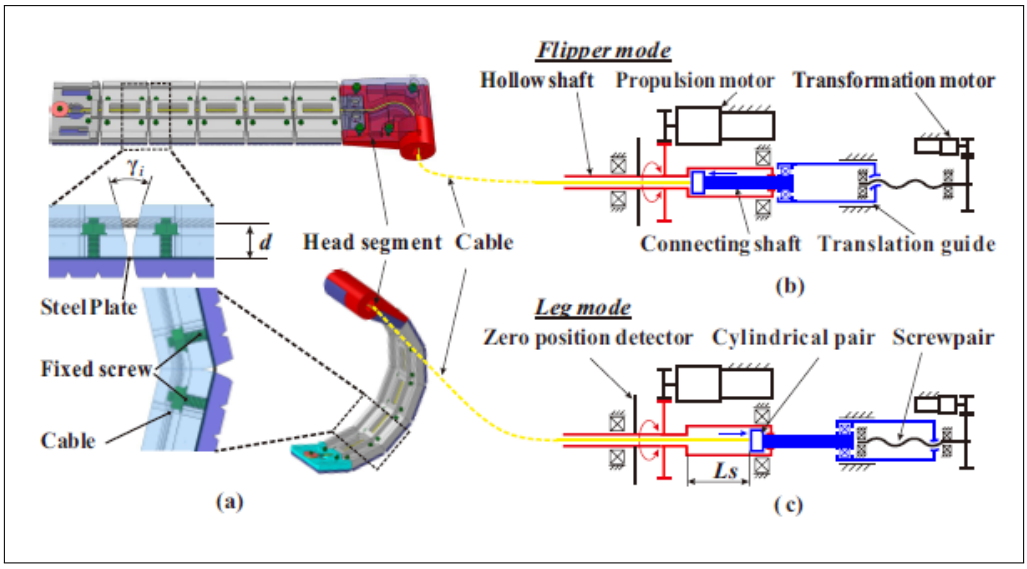

Figure 2.3.3: Mechanical design of the transformable flipper leg. [Zhang et al., 2016]

Another amphibious hexapod robot is AmphiHex-I developed by Zhang et al. [2016]. This vehicle is very similar to AQUA but has legs than can transform from the curved legs used by RHex to flat flipper like appendages that can be used to swim through the water. The vehicle performed well in difficult terrain, passing through soft muddy or sandy bottoms as well as being able to propel itself in water.

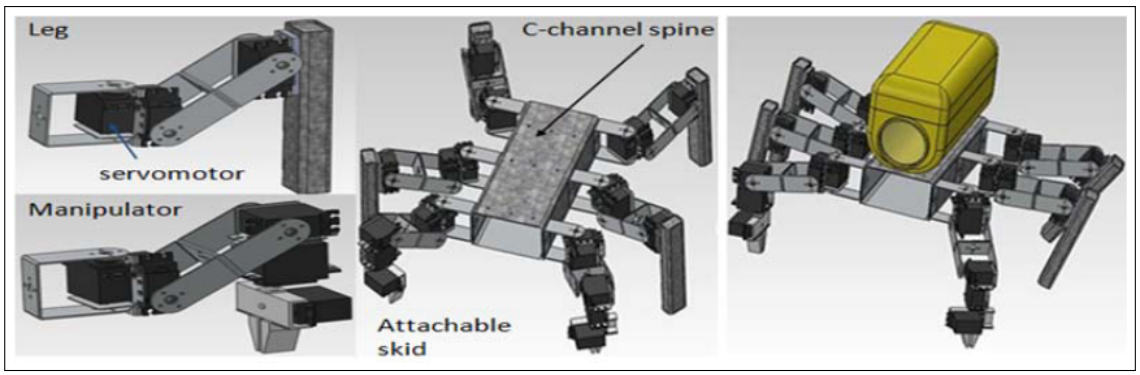

Figure 2.3.4: 3D models of attachable walking skid for sea bed ROV's. [Si and Chin, 2014]

Further research into sub sea walking vehcles lead to the development of the adaptable walking skid by Si and Chin [2014] which also uses the hexapod configuration to move along the sea floor. The skid can be attached to ROV's giving them the ability to walk underwater. The skid has higher degrees of freedom in the legs than seen in Aqua or Amphihex. The skid provides a stable platform that is resistant to seabed currents when performing sub-sea operations such as data collection or pipeline inspection.

Whether crawling or walking, underwater vehicles have trade-offs in obstacle avoidance, payload sizes, mission times, or resistance to currents and waves that make no one vehicle perfect for exploring the surf zone.

2.4 Little Skate

This paper proposes a vehicle inspired by the Little Skate, a batoid found commonly in these kinds of conditions as another possible platform for scientific or military missions in complex near-shore environments. The Little Skate (*Leucoraja erinacea*), shown in Figure 2.4.1, is a cartilaginous fish which inhabits the Atlantic coastline of Canada and the northeastern United States. It is a member of family Rajidae, similar to a ray, it is a batoid with the average male disc breadth and disc length equal to 57.2 and 46.5 percent of the total length which can range from 40cm to 50cm.Bigelow and Schroeder [1953]

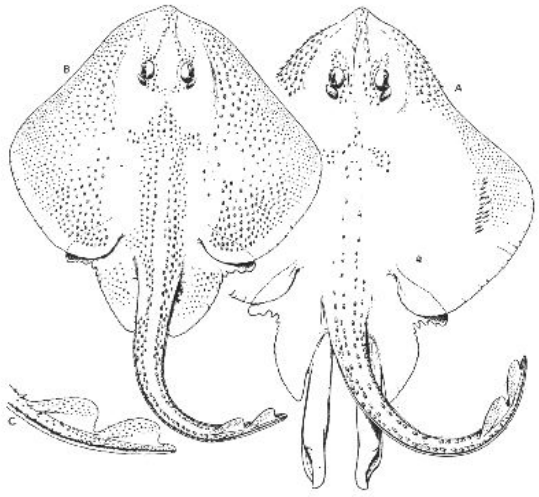

Figure 2.4.1: The Little Skate (*Leucoraja erinacea*). [Bigelow and Schroeder, 1953]

2.5 Punting

The Little Skate spends the majority of its time near the bottom of the water column, either on the sea floor or close to it and uses its pelvic fins in unison to push off the ground and glide forward just above the sea floor [Koester and Spirito, 2003]. Multiple species of benthic batoids use this mode of propulsion, however their kinematics differ between species [Macesic and Kajiura, 2010]. Augmented punters, e.g. the 'Atlantic Stingray' (*Dasyatis sabina*), undulate their pectoral fin as well as their pelvic fins to move forward as opposed to 'true punters' such as the Little Skate. True punters tend to reserve the use of their pectoral fins solely for fast escape maneuvers or obstacle navigation [Koester and Spirito, 2003]. The different punting styles are are reflected in morphological differences; true punters have more specialized muscular and skeletal elements which improve fine motor control during punting and result in faster speeds over ground than augmented punters [Macesic and Kajiura, 2010].

The pelvic fin motion of the Little Skate is shown in Figure 2.5.1. The contact of the pelvic fin with the ground, shown as A in the figure, starts the thrust phase

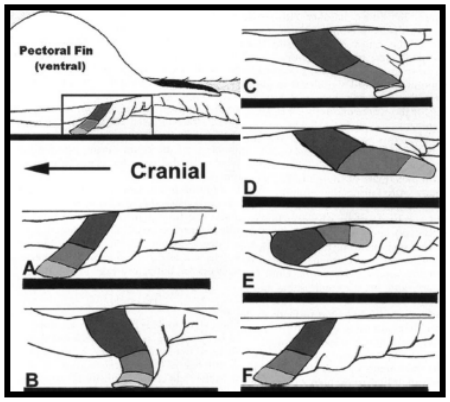

Figure 2.5.1: Motion of pelvic fin [Koester and Spirito, 2003]

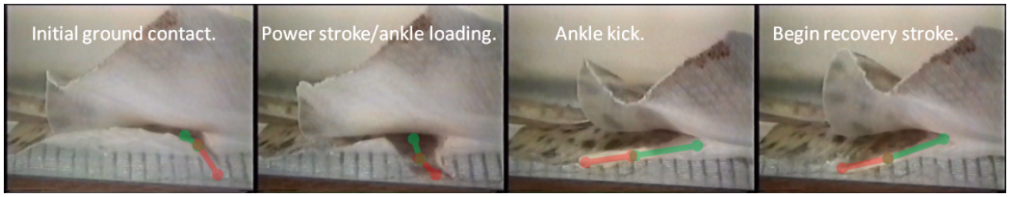

Figure 2.5.2: Video capture of skate punting in a tank seen from below

which lasts until image C, where the fins lose contact with the floor. As the fins leave the ground, image D, the glide phase begins and encompasses the protraction of the pelvic fins, E, and ends when the fins again touch the substrate, beginning the cycle anew. Video taken of a captive Little Skate in a tank show in Figures 2.5.2 and 2.5.3 appear similar to that in Koester and Spirito [2003]. It was also found that Little Skates can reach speeds of about 1/3 body lengths per second using this form of propulsion [Koester and Spirito, 2003]. Both the punting motion and speed provide benchmarks for initial design goals of the vehicle.

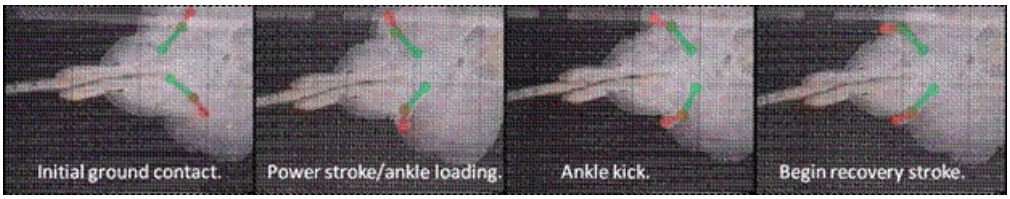

Figure 2.5.3: Video capture of a skate punting in tank seen from the side

CHAPTER 3

Development of the Mechanical Prototype

In order to gain fundamental insight into punting as a method of vehicle locomotion, a legged mechanical prototype was designed and constructed.

3.1 Design and Construction

Table 3.1.1 shows the preliminary goals for the development of the prototype where the first iteration focuses on developing a working punting mechanism with only a few degrees of freedom, mostly passive appendages for stability, and off-board computing and power. The prototype was designed such that various parts of the prototype can be readily changed or replaced to adjust vehicle dynamics.

Prototype Property	**Value**
Body Scale	46cm
Rear Limbs	55cm
Rear Limb DOF	1-2
Forward Body Material	Rigid
Wings	Rigid
Sensors	Pitch angle or nose height
Tail	Passive
Power	Control
Buoyancy	negative
Walking Capabilities	.5 bodylengths/sec
Swimming Capabilities	None

Table 3.1.1: Preliminary 1st Iteration Design Goals

3.1.1 Design of Body and Wings

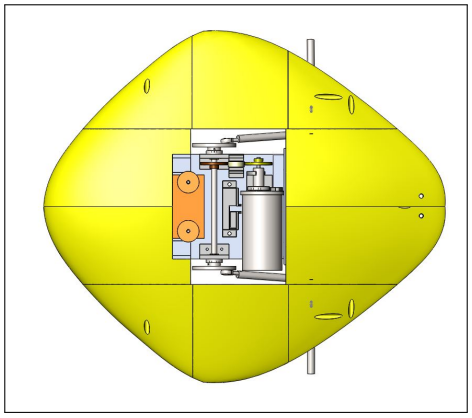

Figure 3.1.1: Top view of punting prototype design

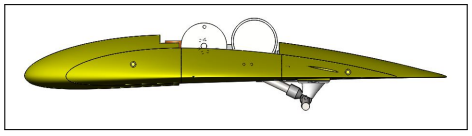

Figure 3.1.2: Side view of punting prototype design

The top profile of the body is a rounded diamond shape with length and width of 70cm and 61cm respectively as shown in Figures 3.1.1 and 3.1.2. The side profile is that of a NACA 4412 airfoil and was chosen for its significant camber to provide increased lift during the glide phase. The body was 3D printed from ABS plastic in ten separate pieces which can then be assembled into four sections: a front section, back section, and the left and right wings. After printing but before being assembled, the pieces were waterproofed by subjecting the parts to an acetone vapor bath which dissolved the outer layer of the ABS pieces enough to allow it to flow and seal the microscopic holes that form between layers during the printing process. The pieces were also covered with several coats of polyurethane and waterproof paint to further prevent water from penetrating into the ABS. Figure 3.1.3 shows a bottom view of the different body pieces including the assembling hardware and removable leg mounts underneath. The propulsion

mechanism is then mounted into the gap left in the center of the assembly.

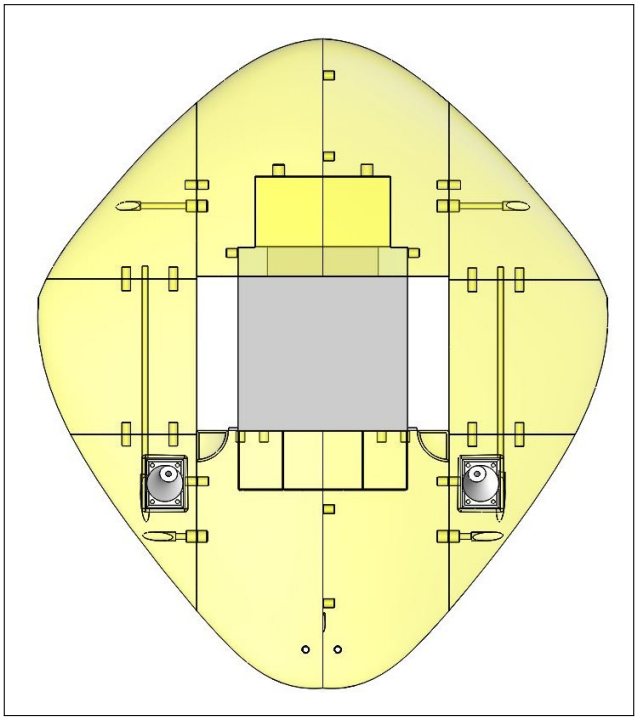

Figure 3.1.3: Bottom view of body wing assembly showing cavities included in the wing for mounting hardware

3.1.2 Propulsion mechanism

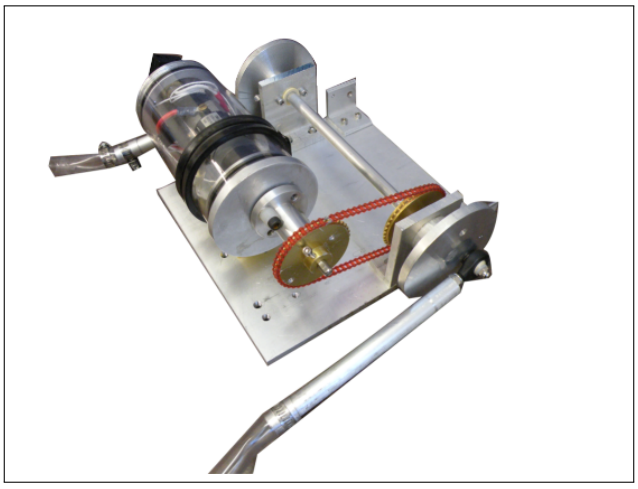

Figure 3.1.4: Image of leg drive system, with upper leg shown as attached to drive disk

Part Number*		C13-L19-				
Winding Code**		10	20	30	40	50
L = Length	inches			1.902		
	millimeters			48.3		
Peak Torque	oz-in	50	50	50	50	50
	Nm	0.353	0.353	0.353	0.353	0.353
Continuous Stall Torque	oz-in	7.5	7.5	7.5	7.5	7.5
	Nm	0.053	0.053	0.053	0.053	0.053
Rated Terminal Voltage	volts DC	6 - 18	6 - 24	6 - 24	12 - 36	12 - 48
Terminal Voltage	volts DC	12	12	24	36	48
Rated Speed	RPM	3000	1880	2875	2225	2877
	rad/sec	314	197	301	233	301
Rated Torque	oz-in	5.8	6.9	6.4	6.7	7.5
	Nm	0.04	0.05	0.05	0.05	0.05
Rated Current	Amps	2.05	1.8	1.4	0.95	1.4
Rated Power	Watts	12.9	9.6	13.6	11.0	16.0
	Horsepower	0.02	0.01	0.02	0.01	0.02
Torque Senstivity	oz-in/amp	3.42	4.35	5.45	8.1	10.25
	Nm/amp	0.0242	0.0307	0.0385	0.0572	0.0724
Back EMF	volts/KRPM	2.53	3.21	4.03	5.99	7.57
	volts/rad/sec	0.0242	0.0307	0.0385	0.0572	0.0723
Terminal Resistance	ohms	1.55	2.30	3.35	7.90	12.00
Terminal Inductance	mH	0.52	0.84	1.30	3.00	4.80
Motor Constant	oz-in/watt^1/2	2.7	2.9	3.0	2.9	3.0
	Nm/watt	0.019	0.020	0.021	0.020	0.021
Rotor Inertia	oz-in-sec^2	.00026	.00026	.00026	.00026	.00026
	g-cm^2	18.4	18.4	18.4	18.4	18.4
Friction Torque	oz-in	0.75	0.75	0.75	0.75	0.75
	Nm	0.01	0.01	0.01	0.01	0.01
Thermal Resistance	°C/watt	11.0	11.0	11.0	11.0	11.0
Damping Factor	oz-in/KRPM	0.1	0.1	0.1	0.1	0.1
	Nm/KRPM	0.001	0.001	0.001	0.001	0.001
Weight	oz	6.8	6.8	6.8	6.8	6.8
	g	193	193	193	193	193
Electrical Time Constant	millisecond	0.3355	0.3652	0.3881	0.3797	0.4000
Mech. Time Constant	millisecond	4.8764649	4.483876	4.152057	4.432363	4.209995
Speed/Torque Gradient	rpm/oz-in	-179.1369	-164.715	-152.526	-162.8228	-154.654

Figure 3.1.5: Motor Specifications [Moog]

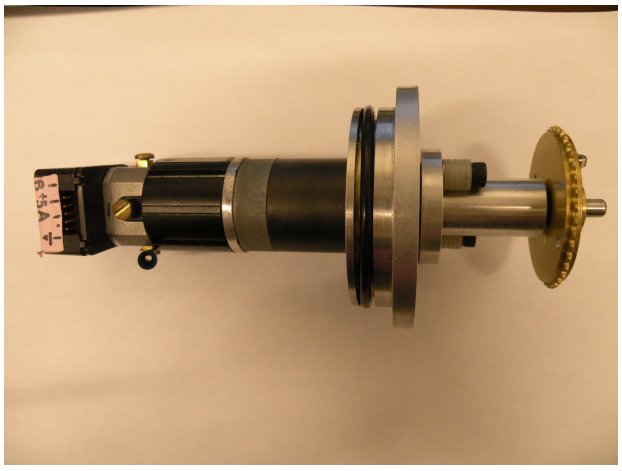

Figure 3.1.6: Motor with mount and gear attached

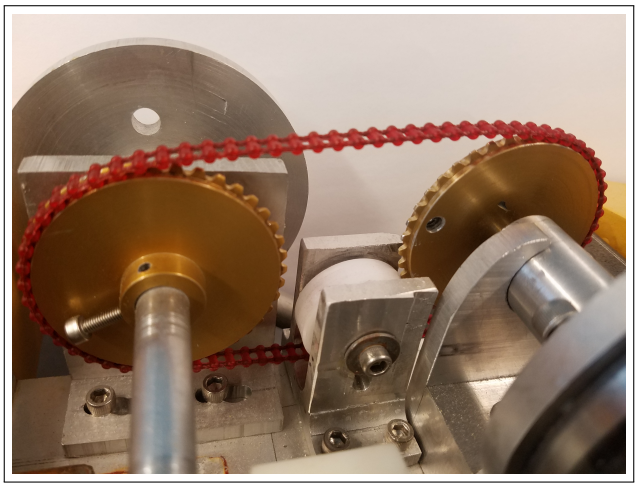

Figure 3.1.7: Drive chain tightener

The propulsion mechanism is shown in Figure 3.1.4. It is powered by a C13-L19-W20 MOOG motor attached to a 51:1 planetary gearhead and HEDS 5500-500 optical encoder. The specifications of the motor are listed in the highlighted column of Figure 3.1.5. The motor, installed in a waterproof housing, is geared to the axle that drives the two discs attached to two linkages. To maintain a taught chain, a tightener was added to the vehicle, seen in Figure 3.1.7. The linkages translate the rotary motion of the disks to a linear reciprocating motion that drives the under wing appendages shown in Figure 3.1.8. As the exterior wheels turn, the linkages flap the appendages back and forth in a sinusoidal motion constrained by specially designed removable mounting points on the underside of the wings. These mounts are designed with a $-5°$ slope from the center of the body toward the wings and a $-23°$ slope from nose to tail. This geometry causes the tip of the appendage to impact the ground, lifting the vehicle and propelling it forward. The motion of these appendages can be seen in the sequence of images in Figure 3.1.9. These are mounted to the underside of the wings on both sides and connected to the linkages by a flexible universal joint. The exact location in space of these appendages can be calculated by finding the the intersection of two spheres and a plane. Each sphere

represents the length of each segment from its mounting point and the plane being the plane of the 3D printed underwing mounts. A visualization of the problem can be seen in Figure 3.1.10. The solution is plotted in 3 dimensions in Figure 3.1.11.

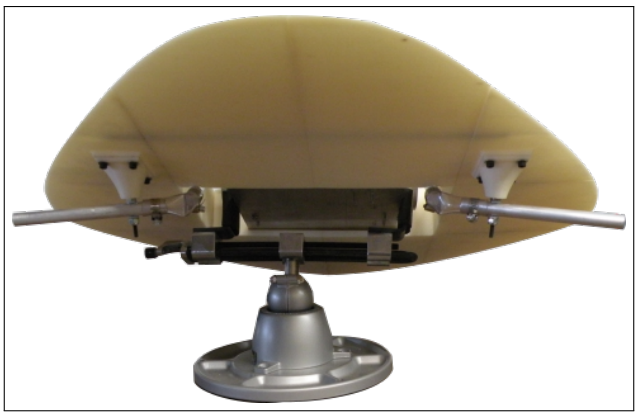

Figure 3.1.8: Image of bottom of vehicle prior prior to sealing and painting, showing the underwing mount points for the legs

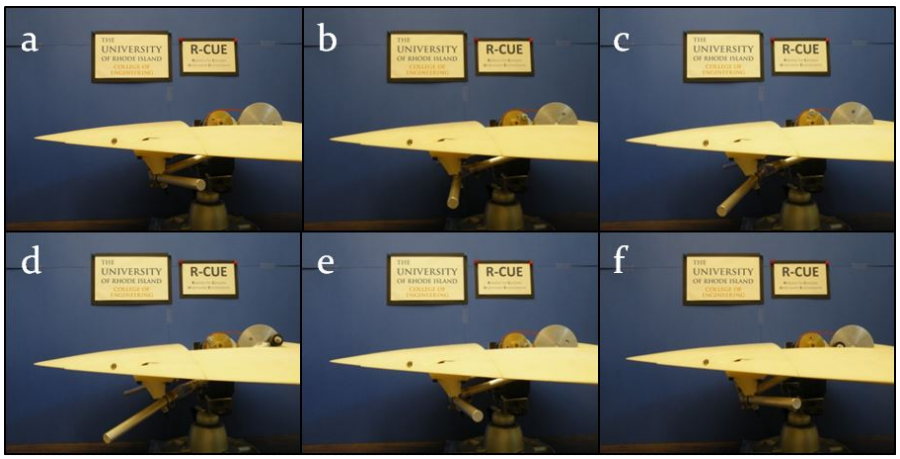

Figure 3.1.9: Motion of the underwing appendages

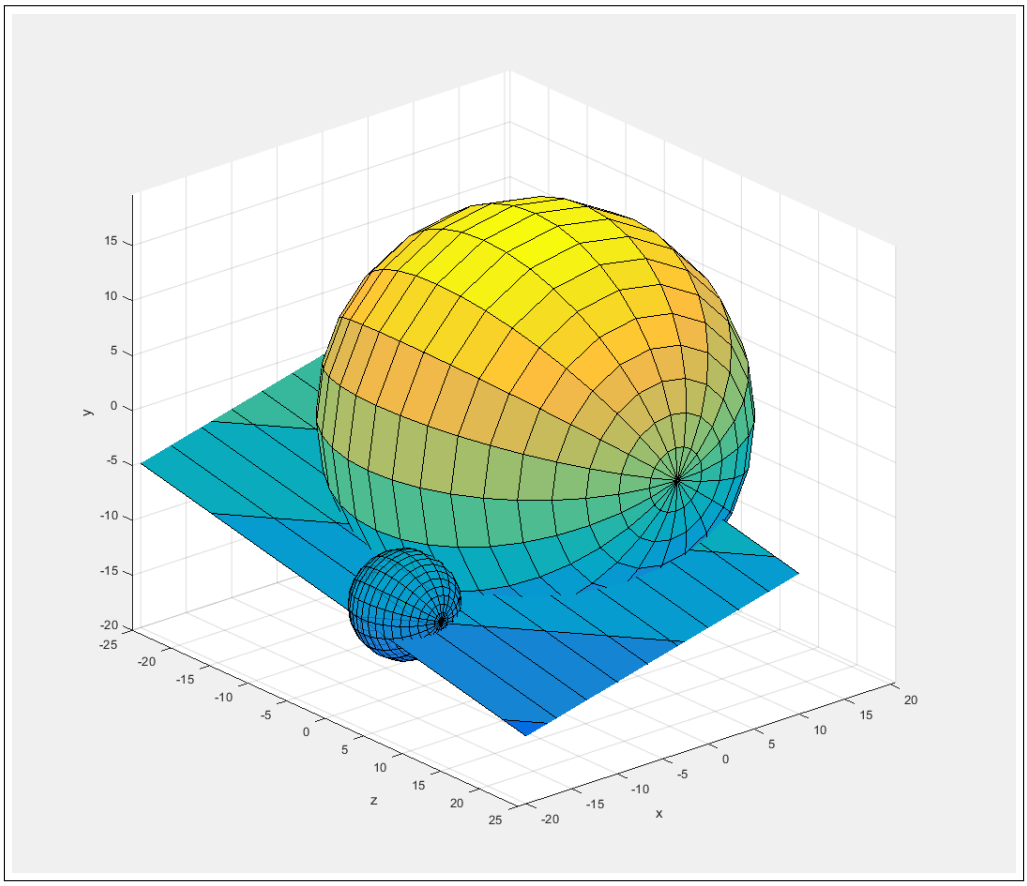

Figure 3.1.10: Visualization of leg motion solution

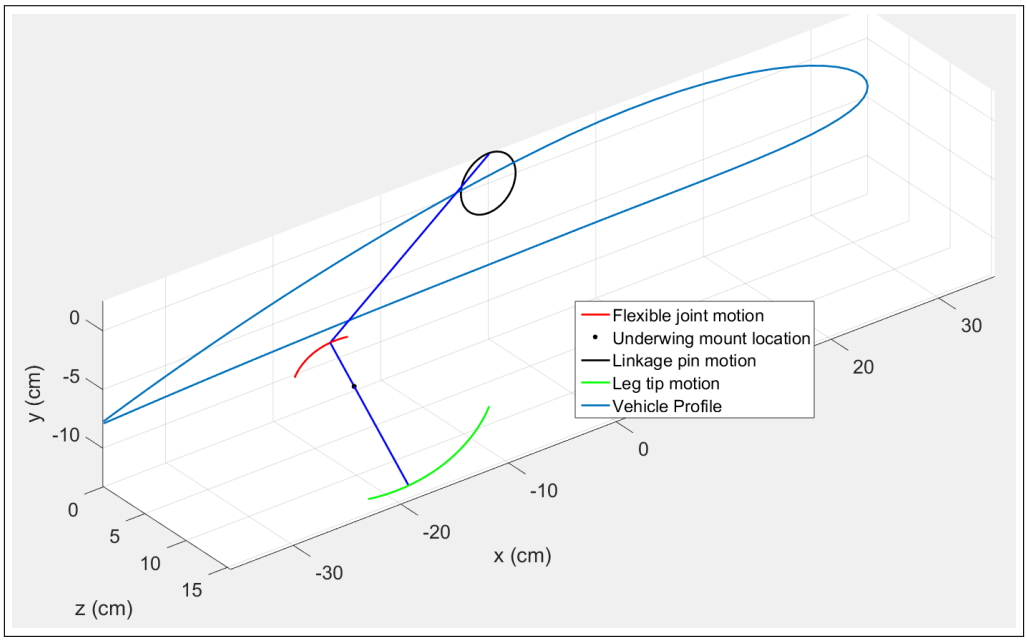

Figure 3.1.11: Motion of the leg segments

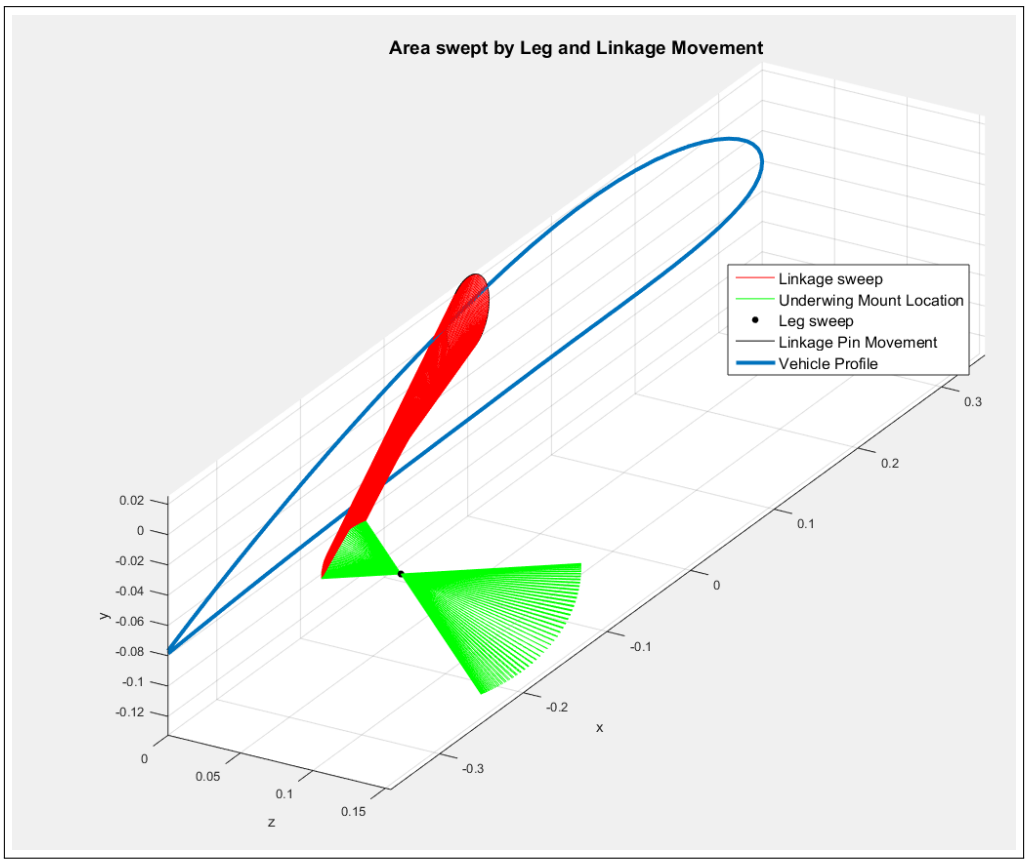

Figure 3.1.12: Swept area of the motion of the leg segments

3.1.3 Waterproof Housing

The motor's waterproof housing is an acrylic tube with two aluminum end caps containing o-ring seals. The stock shaft of the motor was not long enough, so a coupler and shaft extension was added. To waterproof the shaft, a shaft seal mount, shown in Figure 3.1.14, was designed to hold a shaft seal as well as contain the shaft coupler when bolted to the face of the forward end cap. The cavity in Figure 3.1.14a holds the shaft seal and the cavity in figure 3.1.14b is where the coupler is located an the entire cavity is also packed with marine grease. The interface between the shaft seal mount and the end cap is sealed with a rubber flange. Figure 3.1.15 shows an exploded view of the entire waterproof housing assembly as well as the mounting device that hold the housing to the body of the vehicle and adds additional support to the shaft seal mount. Finally, figure 3.1.16 shows the underwater connectors added to the back end cap in order to connect to the motor and encoder inside the housing.

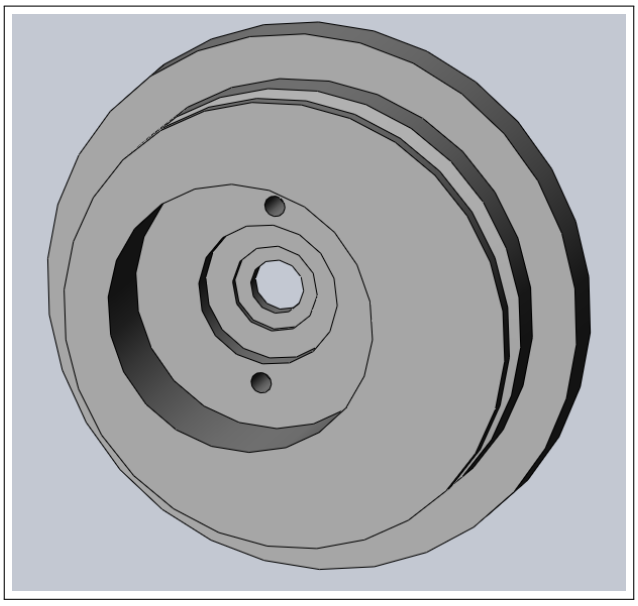

Figure 3.1.13: Solidworks rendering of end cap with o-ring seal and integrated motor mount for drive motor

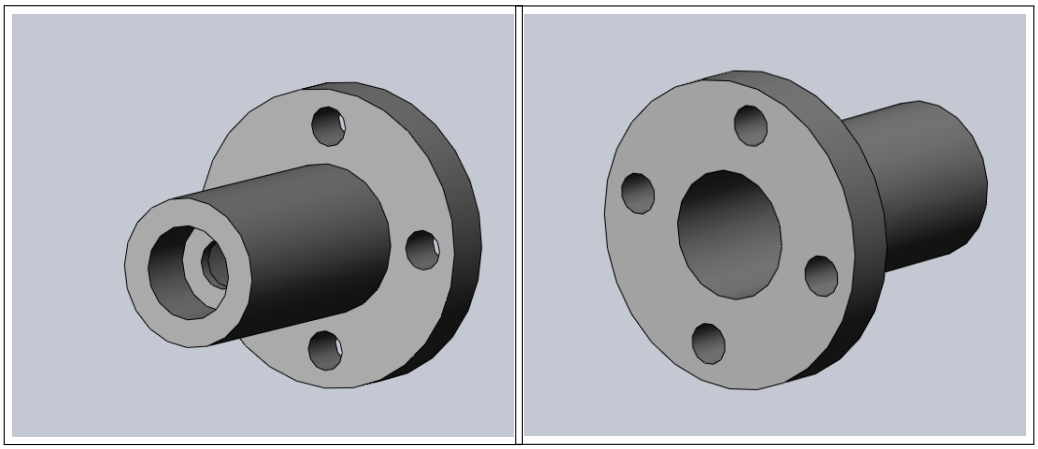

(a) Front (b) Back

Figure 3.1.14: Solidworks rendering of grease filled shaft seal mount

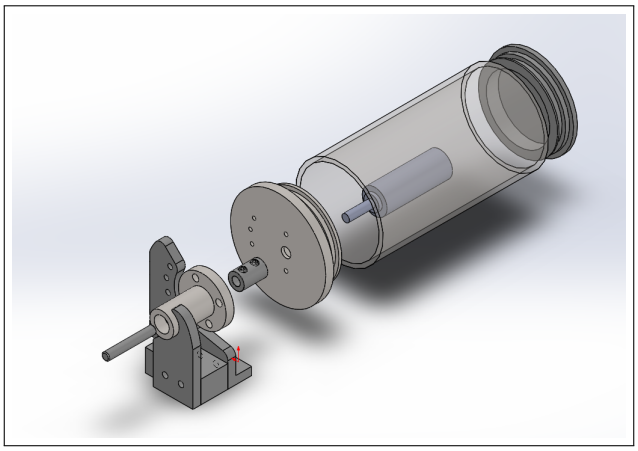

Figure 3.1.15: Exploded view showing the waterproof housing with the motor, shaft extension coupler, grease packed shaft seal mount, o-ring sealed end caps and the housing mount

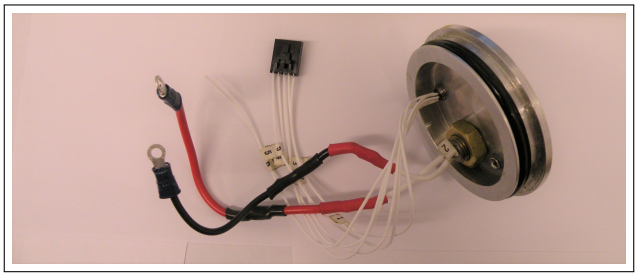

Figure 3.1.16: Underwater connectors for power to the motor and encoder installed in one end cap

3.1.4 Buoyancy and Center of Gravity

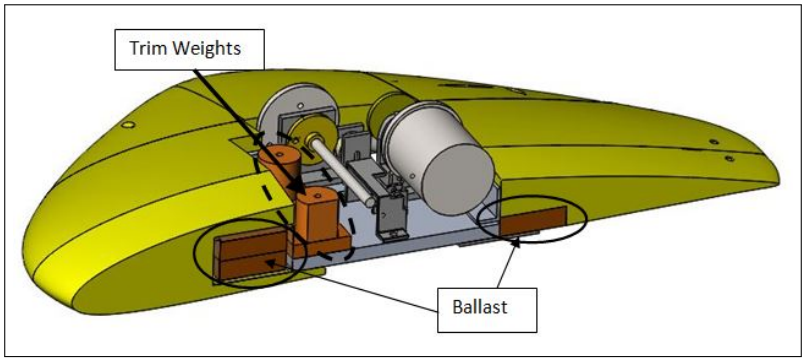

Figure 3.1.17: Cutaway view showing mount locations for ballast and trim weights

The ABS plastic that makes up the body and wings is 3D printed in a honeycomb configuration to minimize material. The resulting structure is positively buoyant. The buoyancy of the ABS sections is counteracted by installing steel weights as ballast inside the forward and aft pieces (circled in Figure 3.1.17). This ballast makes the vehicle approximately neutrally buoyant, then secondary weight is added to the top of the vehicle (circled by the dashed line in Figure 3.1.17). For all tests described, the vehicle was slightly negatively buoyant with the center of gravity above and forward of the underwing appendage mounts. The center of buoyancy and center of gravity, illustrated in Figure 3.1.18, are offset horizontally to create a hydrostatic moment that lifts the nose of the vehicle off the ground. A compliant tail is used to oppose hydrostatic moment while the vehicle is stationary and create a consistent initial pitch angle when the vehicle is at rest.

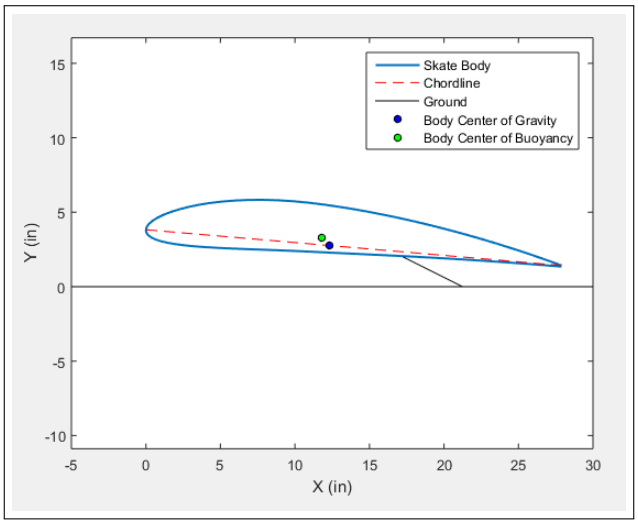

Figure 3.1.18: Vehicle Center of Gravity and Buoyancy

3.1.5 Tail

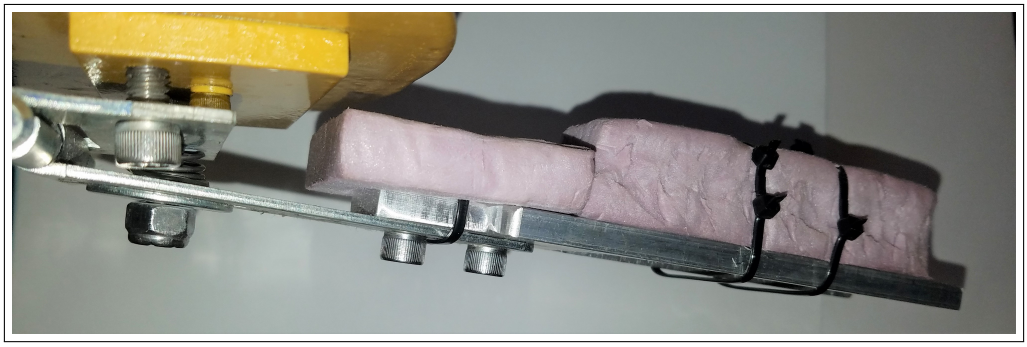

Figure 3.1.19: Tail mechanism attached to the bottom of the vehicle

To counteract the hydrostatic wrench of the centers of gravity and buoyancy a 'tail' was attached to the vehicle, shown in Figure 3.1.19. The tail is a metal plate on a hinge that extends downwards and backwards from the back of the vehicle. When the vehicle is at rest it reaches an equilibrium between the spring in the tail and the hydrostatic wrench where the vehicle has a constant pitch angle before the legs kick. The tail also tends to impact the floor as the vehicle glides downwards. The spring in the tail works to soften the impact, decreasing any jerks imparted on the vehicle. The tail is also equipped with foam to make it neutrally balanced

to eliminate any gravitational forces from the tail on the body.

3.1.6 Electronics and Wiring

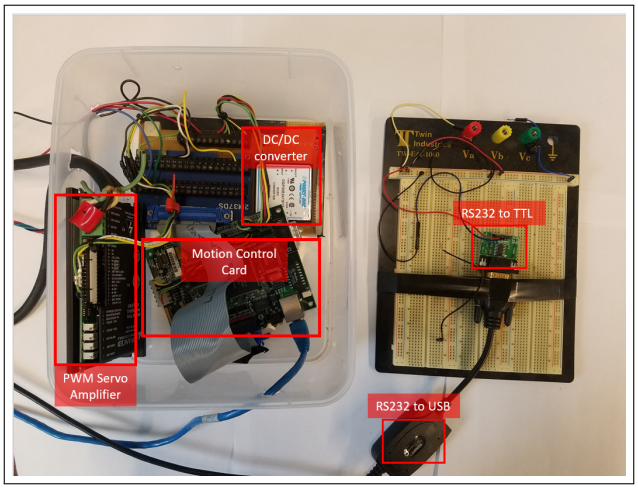

Figure 3.1.20: Onshore Electronics

On board the vehicle is the motor and a Vector Navigation VN-100 inertia measurement unit. The onshore half of the system is shown in Figure 3.1.20. The system consists of a Galil DMC-1425 motion control card, an Advanced Motion Control 25A model 12A8 PWM Servo amplifier, and a DC/DC Converter. These parts are wired as shown in Figure 3.1.21. The signal from the on-board IMU is passed to the RS232-TTL converter also shown in Figure 3.1.20 which is in turn converted to USB protocol before sent to a computer to be recorded.

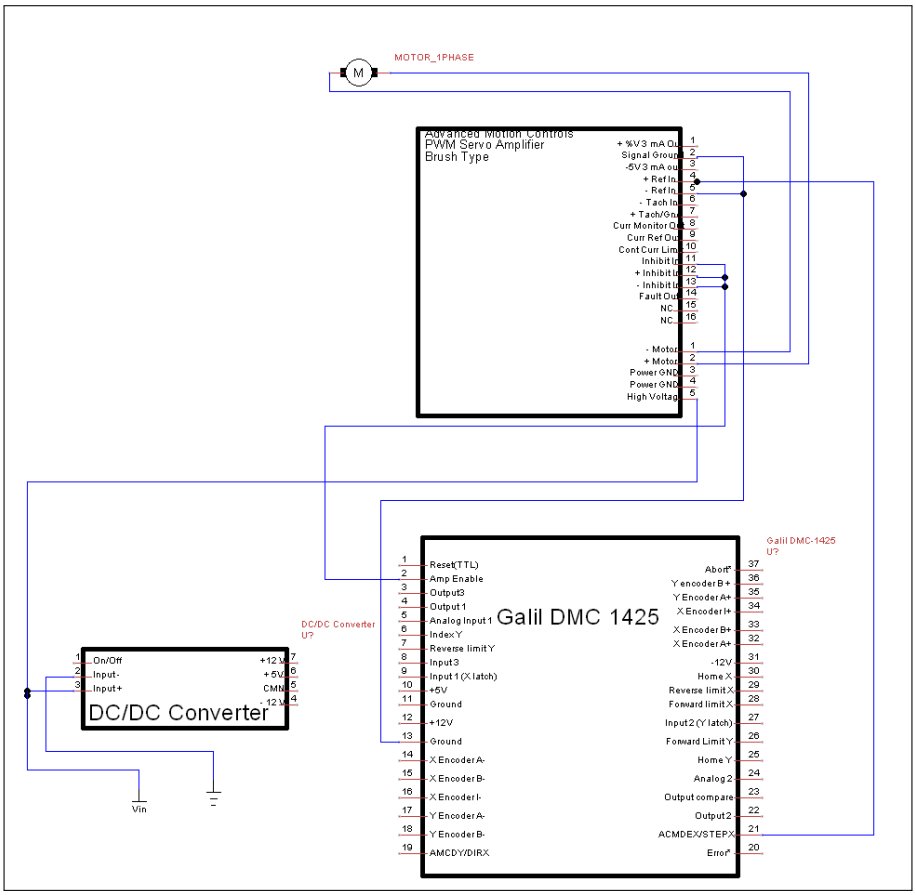

Figure 3.1.21: Wiring diagram of the skate vehicle

3.2 Testing

In order to evaluate the performance of the mechanical prototype it was subjected to in-water trials at the University of Rhode Island wave tank facility. A characteristic motor speed of two revolutions per second was chosen and the vehicle was run for two successive kick cycles with a varying pause length between the cycles. Initial tests were limited to two kicks due to limits imposed by the field of view of the camera and to limit the effect of variations in the (uncontrolled) yaw motion. The vehicle was run 12 times for each case and all the trajectories for each respective pause length were averaged together. The difference in delay or pause length can be visualized in the motor position and speed profiles shown in Figures 3.2.1 and 3.2.2. The test runs are tabulated below in Table 3.2.1

[H]

Table 3.2.1: Test Runs

Motor speed	$200,000 \frac{cnts}{s} \approx 2 \frac{rev}{s} \approx 1Hz$
Delays	800ms, 900ms, 1000ms, 1100ms, 1200ms
Number of Trial per Run	12

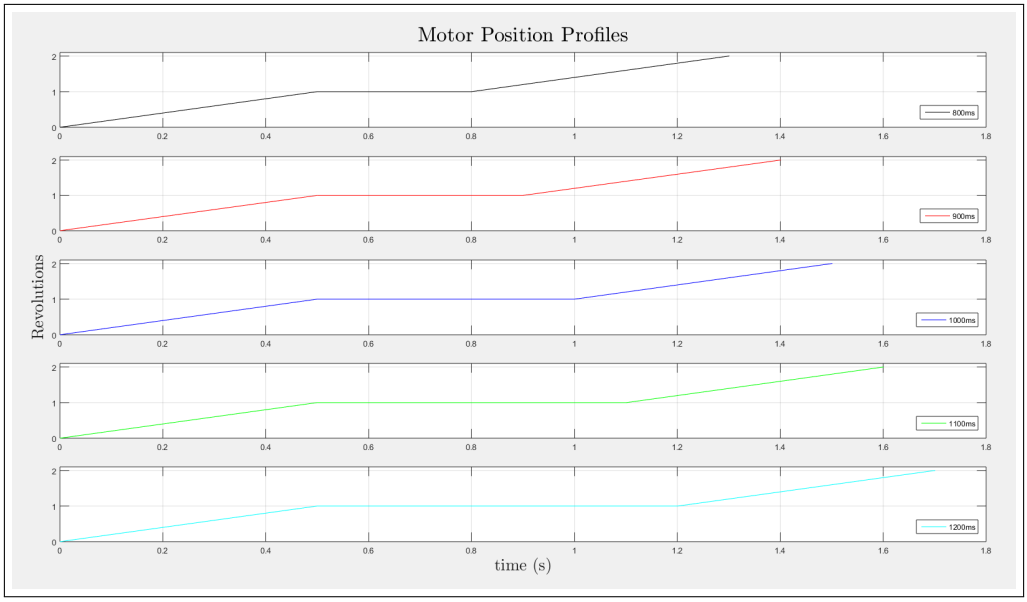

Figure 3.2.1: Motor position profiles for different runs

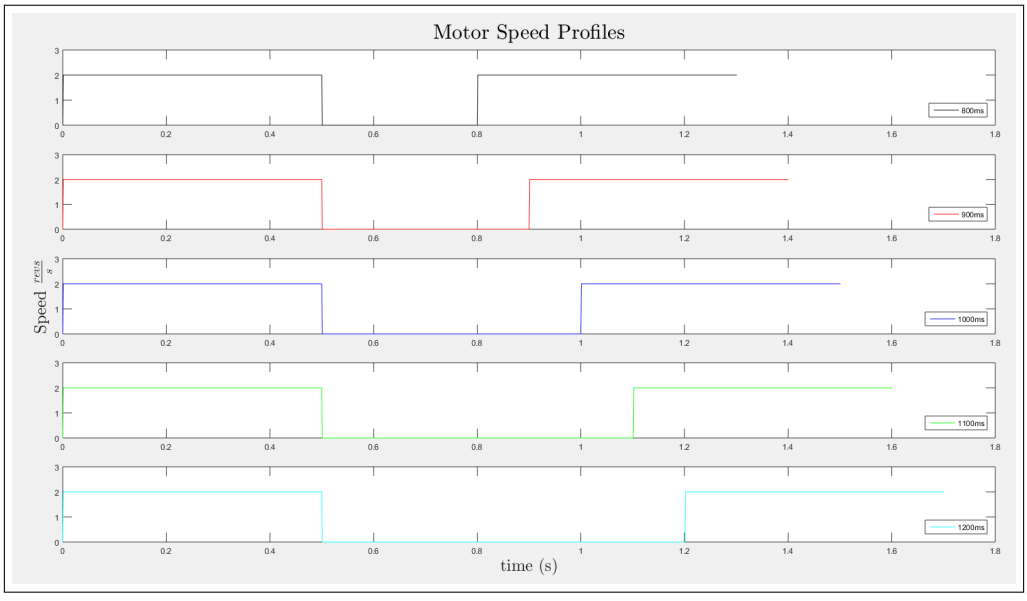

Figure 3.2.2: Motor speed profiles for different runs

3.2.1 Experimental Test Setup

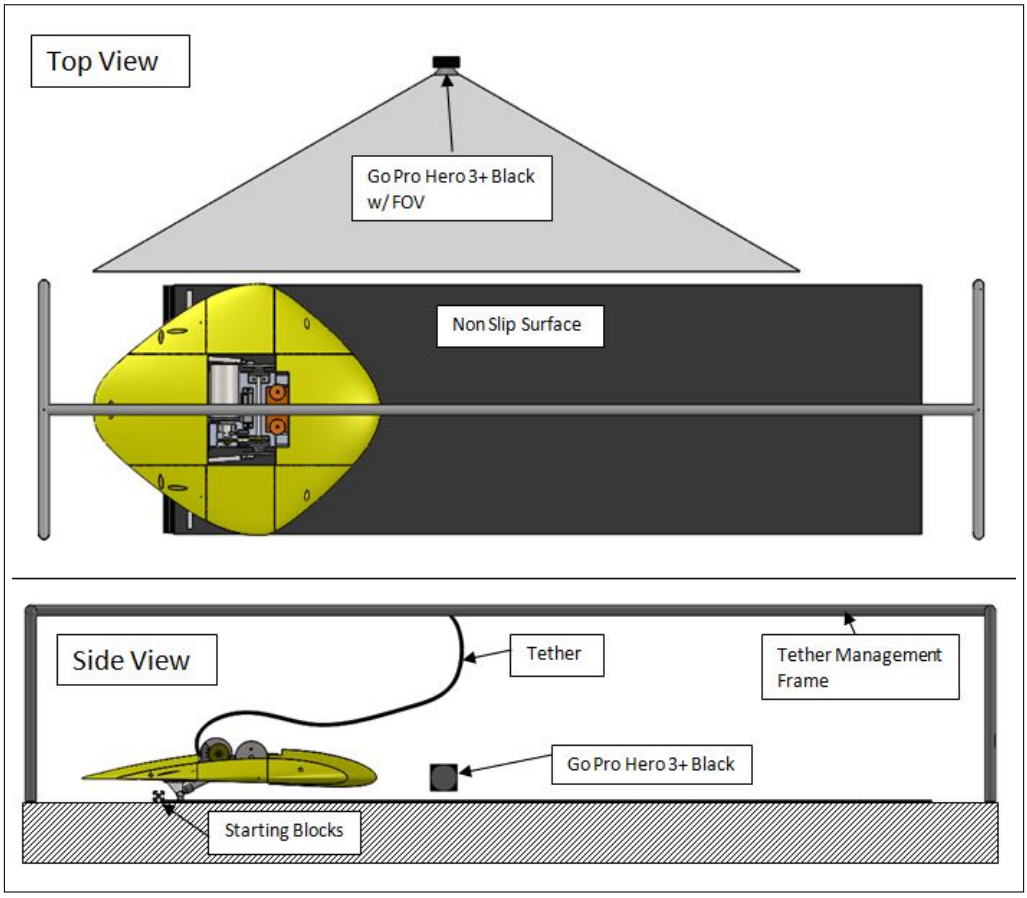

Figure 3.2.3: Schematic of experimental setup

The experimental setup is shown in Figure 3.2.3. The vehicle was placed on a solid, level floor covered with a non-slip material for the vehicle feet. Starting blocks were added to provide a repeatable kickoff and the scaffolding above the test area was used for tether management. The tether was required to provide power and communication to both the motor and on-board sensors.

3.2.2 Data Analysis

The vehicle trajectory was captured with a Go-Pro 3+ video camera and then the motion was extracted from the video using a Speeded Up Robust Feature (SURF) tracker. The Go-Pro has a fish eye lense allowing it a larger than

normal field of view, however the distortion must be removed before an analysis can be done on the video. Using multiple calibration images such as that in Figure 3.2.4 and MATLAB's camera calibration tool to estimate the camera's intrinsic properties and distortion as well as remove them from the video recorded. Using MATLAB's computer vision toolbox SURF features from each frame were able to be extracted and tracked in order to record the motion of two points on the vehicle through time. An example of the SURF features that could be found is shown in Figure 3.2.5. The two chosen features for tracking are depicted in Figure 3.2.6. Knowing the exact distance from the camera to the points as well as the locations of the points on vehicle the position and orientation of the vehicle in space can be calculated.

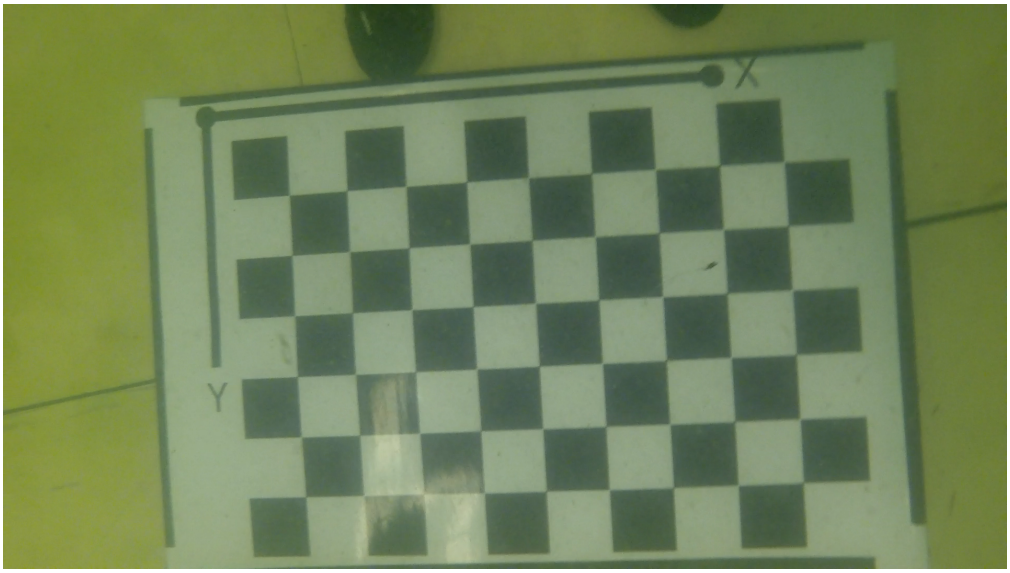

Figure 3.2.4: Example image used for camera calibration.

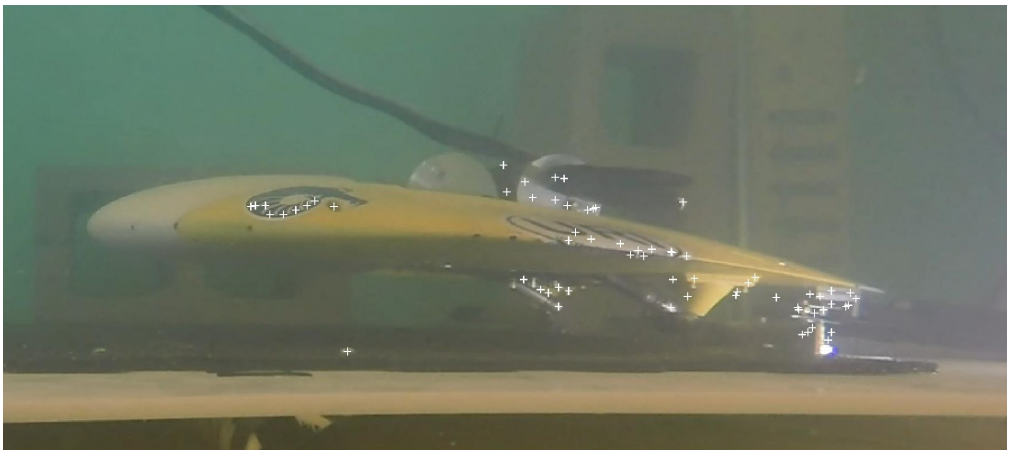

Figure 3.2.5: One frame from trial video showing tracking features detected on the vehicle.

Figure 3.2.6: Image showing chosen features that were tracked through the video.

3.3 Results

Table 3.3.1: Final Prototype Vehicle Specifications

Body Length	$70cm$
Body Width	$60cm$
Vehicle Mass	$10.995kg$
Total Vehicle Volume	$0.0105m^3$
Total Buoyant Force	$103.288N$
Vehicle weight in water	$4.573N$
Body Side Profile	NACA 4412
Center of Gravity	$0.324m$ from the nose
Center of Buoyancy	$0.300m$ from the nose
Upper linkage length	$0.184m$
Lower appendage Length	$0.152m$
Foot Excursion Distance	$0.120m$

The final vehicle specification are listed in Table 3.3.1. Figures 3.3.1, 3.3.2, 3.3.3, and 3.3.4 show 12 frames from the video captured during a trial from each of the separate runs after being undistorted. The images illustrate the movement of the vehicle over two kick strokes and two glide phases. From the video it can be seen that the vehicle motion is the same for the first kick. By 0.5 seconds the legs have kicked backwards and propelled the vehicle into its first glide. The leg of the vehicle can be seen by 1.25 seconds to be in different phases of its kick cycle depending on the kick delay of each trial. In figures 3.3.3 and 3.3.4 the vehicle can be seen to land after the second kick with the trials with longer delays landing last. These images also show evidence of some roll instability which will cause some error in the pitch and height data extracted from the video.

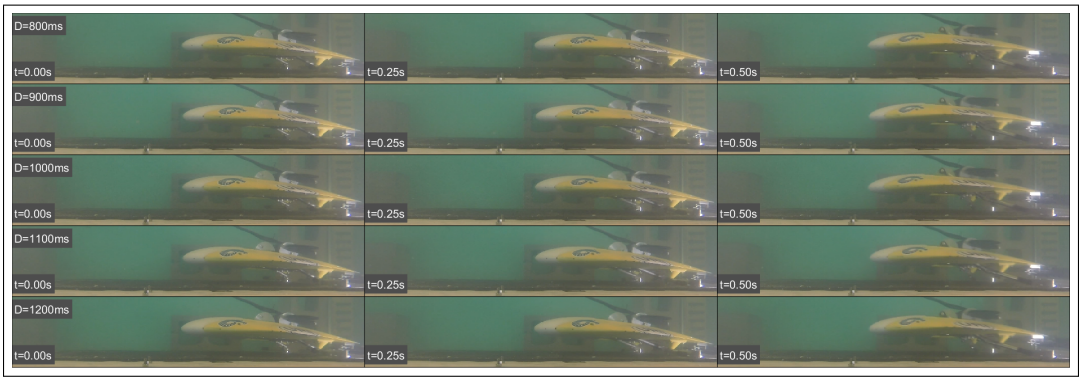

Figure 3.3.1: Still frames extracted from video of trials, time 0 to .5s

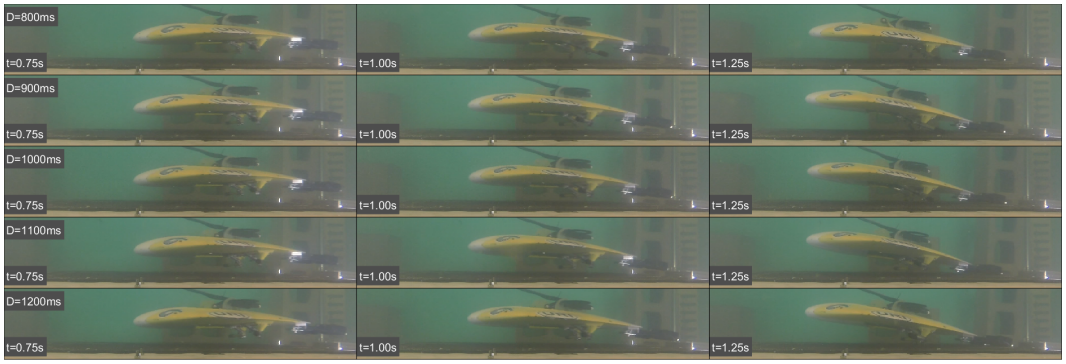

Figure 3.3.2: Still frames extracted from video of trials, time .75 to 1s

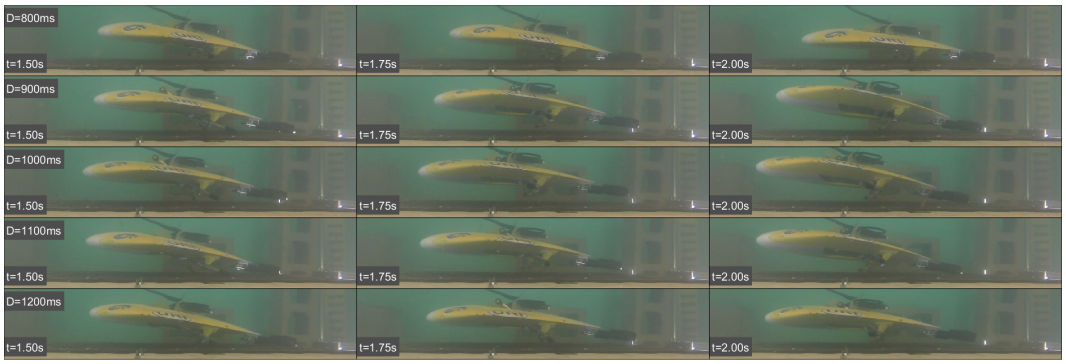

Figure 3.3.3: Still frames extracted from video of trials, time 1.25 to 1.5s

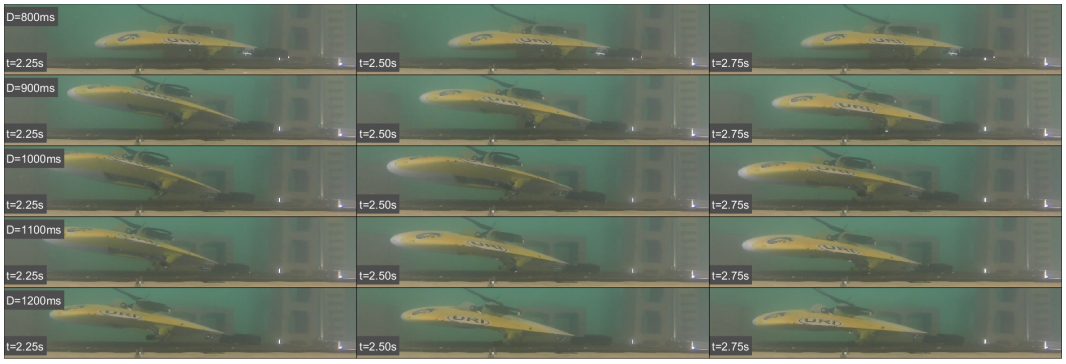

Figure 3.3.4: Still frames extracted from video of trials, time 1.75 to 2s

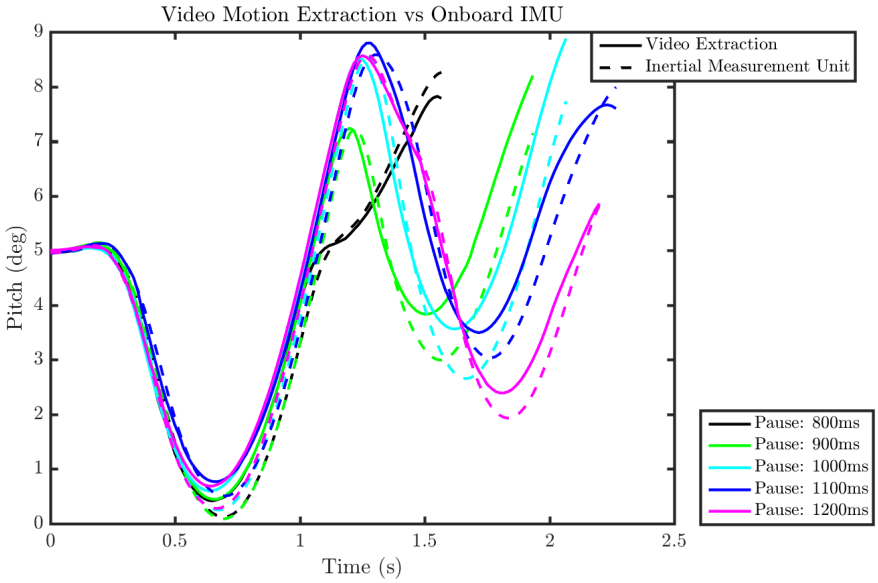

Figure 3.3.5: Comparison of feature tracking pitch and IMU pitch

To validate the motion capture algorithm, the pitch of the vehicle was calculated from the feature tracking data and compared to the on-board IMU pitch signal. These comparisons are shown in Figure 3.3.5 for the different trials. A tendency for the vehicle to yaw toward the camera during the second kick leads to some error in the pitch derived from the video data. The error in pitch does not exceed one degree over the course of two glides but, the use of multiple cameras to provide a full 3D motion capture capability is anticipated in future efforts.

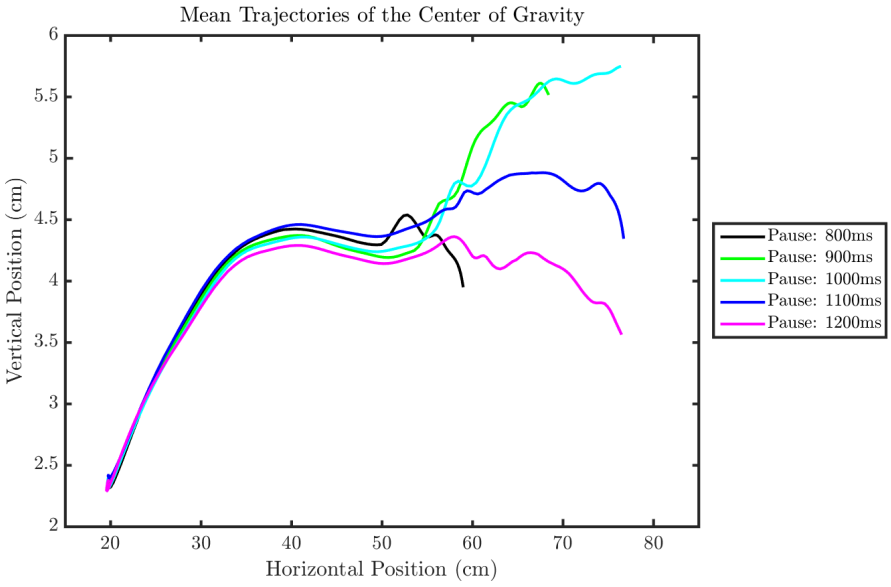

Figure 3.3.6: Mean vehicle trajectories for different pauses

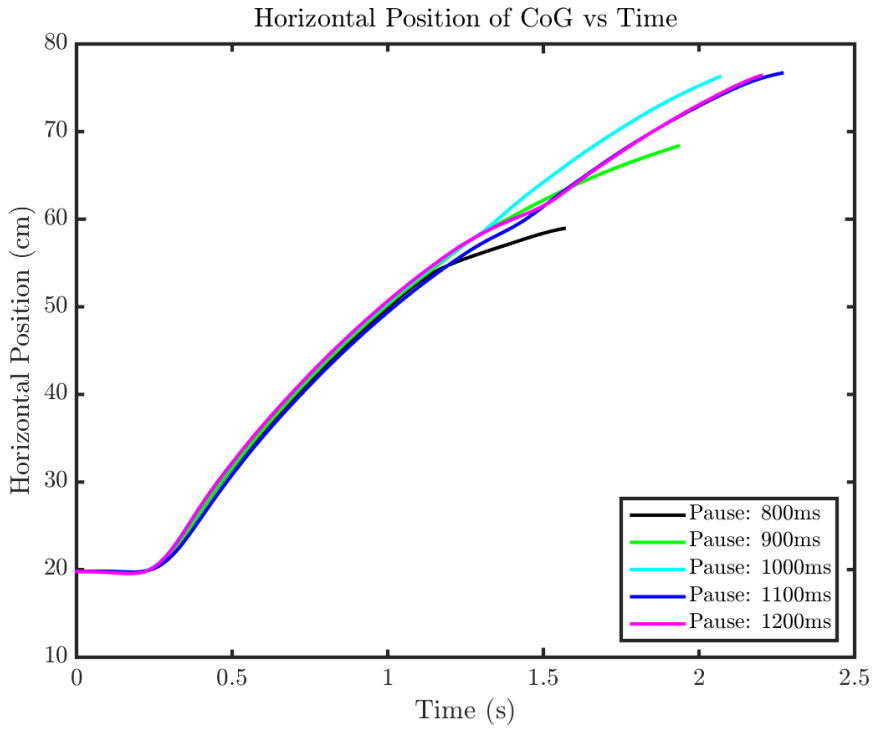

Figure 3.3.7: Mean horizontal distance over time of different pauses

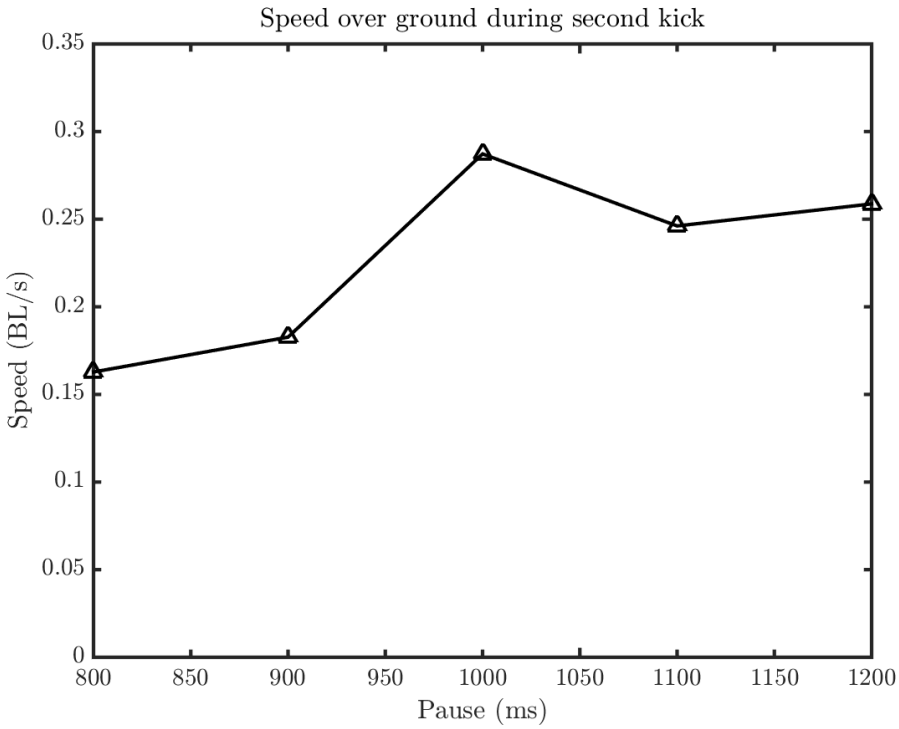

Figure 3.3.8: Average speed over ground during the second kick and glide phases

The vehicle's trajectories and speeds are plotted versus their respective pause lengths in Figure 3.3.6 and Figure 3.3.8. The vehicle reaches a max of 8.5 degrees of pitch over the two kicks and a minimum of zero degrees. The horizontal travel of the center of gravity ranges from 40cm to about 65cm during a run. Average speed over ground for the runs is shown in Figure 3.3.8. The speeds range from 0.163 body lengths per second (BL/s) to 0.2873BL/s with the highest average speed occurring with a pause length of 1000ms.

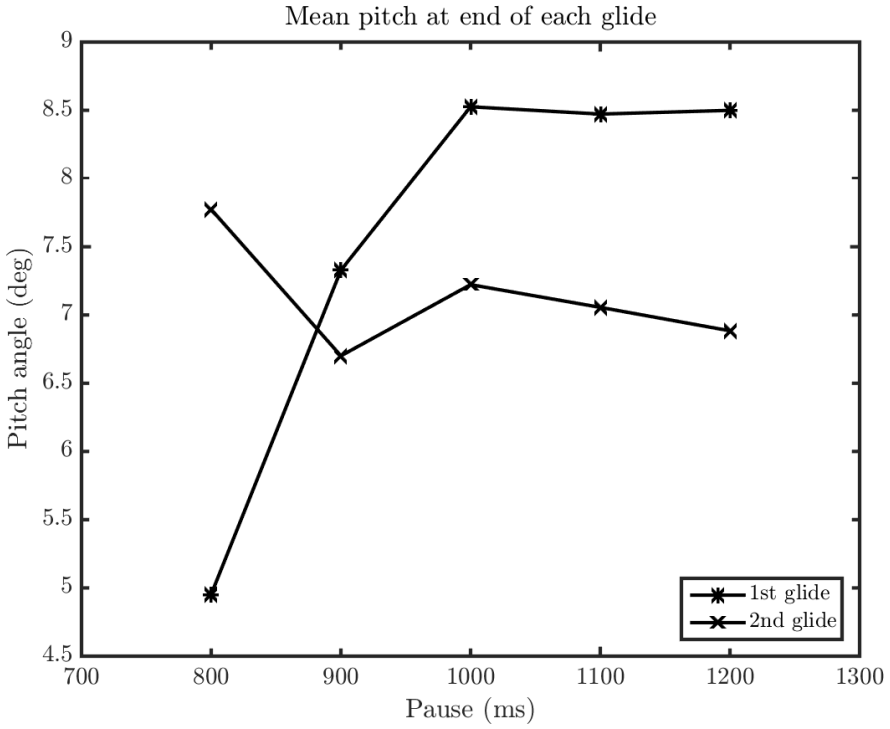

Figure 3.3.9: Mean pitch at end of second glide phase with respect to the mean pitch at the end of the first glide phase

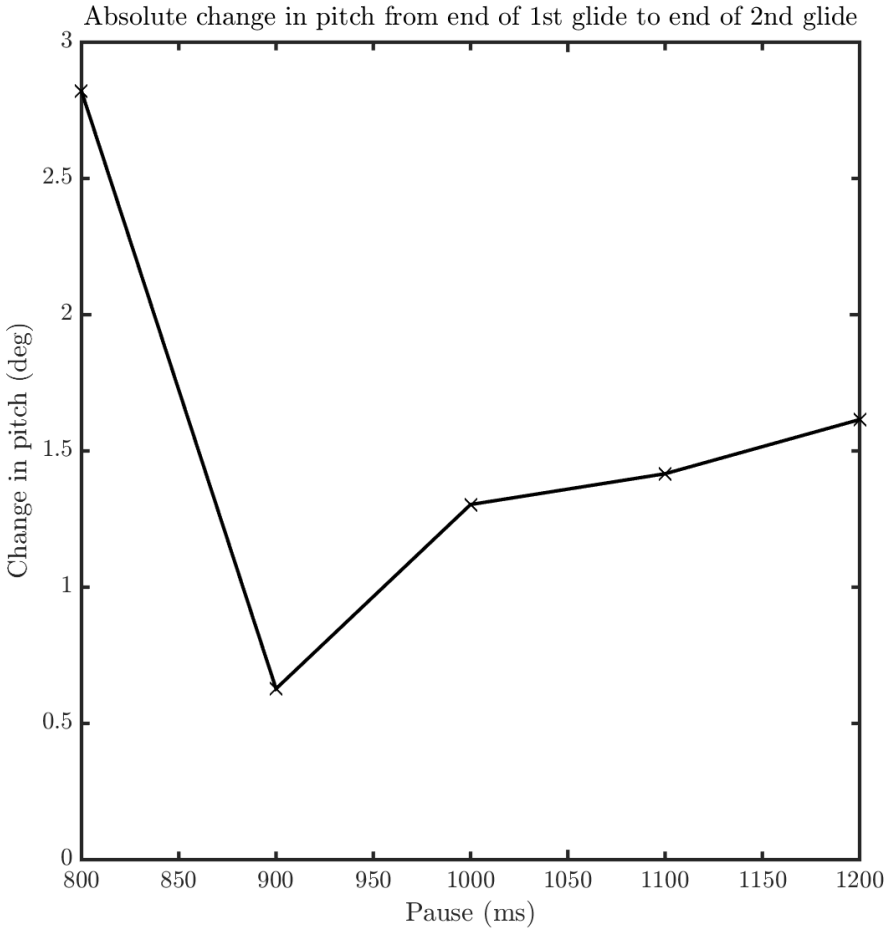

Figure 3.3.10: Change in pitch over 2nd kick and glide phase

Figure 3.3.9 and Figure 3.3.10 compare the pitch angle of the vehicle at the end of each glide phase, showing both and the absolute change between the two, respectively. The greatest change occurs with a pause of 800ms and this is also the only run with a negative change. The others all have a positive change.

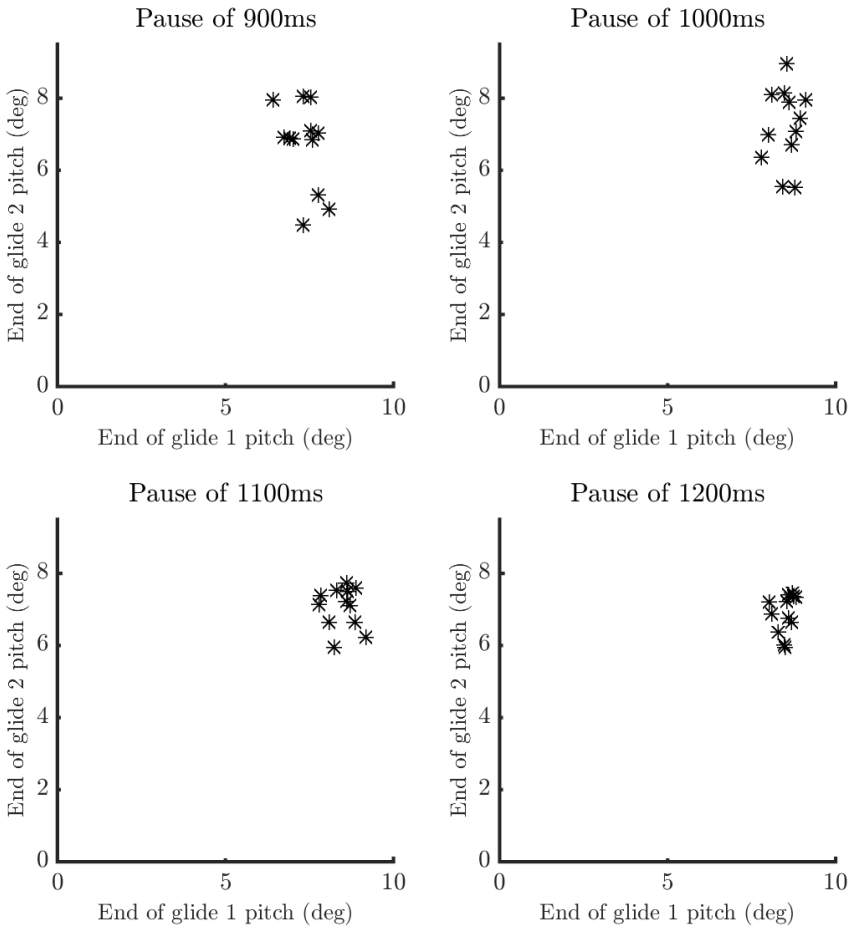

Figure 3.3.11: Mean pitch at end of second glide phase with respect to the pitch at the end of the first glide phase as it changes with pause length

Figure 3.3.11 compares all 12 trials for each run from pause length of 900ms to 1200ms. This figure shows a plot of the pitch at the end of the first glide versus the pitch at the end of the second glide. A tight cluster corresponds to a higher repeatability in the second kick and glide phases. The pause length of 1200ms was found to have the tightest cluster of trials and therefore the greatest similarity in movements across all trials.

3.4 Discussion

From these results the following can be shown:

1. Different pause lengths have a significant effect on the trajectory and speed over ground of the vehicle.

2. The vehicle does not passively return to the same pitch at the end of each kick and glide phase.

3. Ground contact between successive kicks affects the repeatability of the kick and glide phase motions.

The different pause lengths have a considerable effect on the trajectory of the vehicle. If the pause is too short, the feet will not contact the ground. If the pause length is too long the vehicle will contact the ground before kicking, effectively halting the forward motion of the vehicle, as seen in Figure 3.3.7. Figure 3.3.8 shows a peak in speed over ground at a pause length of 1000ms and shows a trend of increasing speed over ground with an increase in pause length. For the longer pauses, the vehicle pitches down after leg contact so that when the legs kick, it propels the vehicle at a lower angle, as can be seen in the trajectories in Figure 3.3.6.

To achieve stable, steady propulsion the vehicle must return to its initial pitch angle over the kick and glide phase. Figure 3.3.9 and Figure 3.3.10 show the change in pitch over the second kick and glide phases. The pause length which corresponds with maximum speed over ground also leads to large changes in pitch between successive kicks which impedes further motion. A pause length of 900ms shows the smallest change in pitch angle but achieves a lower speed over ground than the other pause lengths.

Figure 3.3.11 shows the representative return maps for multiple pause lengths. The spread decreases as the pause length increases which appears to indicate that at longer pause lengths the vehicle spends more time in contact with the bottom

which levels out any variations in roll and pitch that occurred while the vehicle was gliding and the vehicle begins to return to its static initial orientation before the legs come in contact with the ground initiating the second kick phase. While this provides a repeatable kick and glide phase, it is not energetically desirable as it implies a stop-start motion with energy lost at every contact.

CHAPTER 4

Introduction of a Practical Modeling Approach for a Punting Vehicle

From the video collected in the testing of the prototype, the motion of vehicle could be separated into different phases. Each of these phases require their own model to predict the motion. Figure 4.0.1 shows the cycle of the motion divided into separate phases. Figures 4.0.2, 4.0.3, 4.0.4, and 4.0.5 show each phase in more contact. The glide phase has a simpler projectile motion model, while the tail contact and mount contact phases can be modeled as inverted pendulums and the punting phase can be modeled also as an inverted pendulum but with a changing pendulum length. The glide phase, being the simplest was the first to be modeled and compared to the experimental data before models of the others are developed.

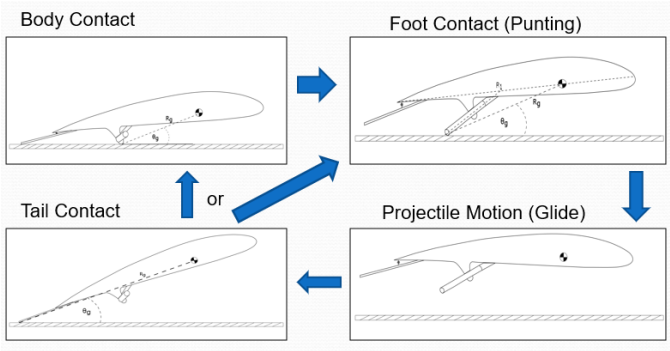

Figure 4.0.1: Cycle of phases vehicle will pass through, each needing a separate model

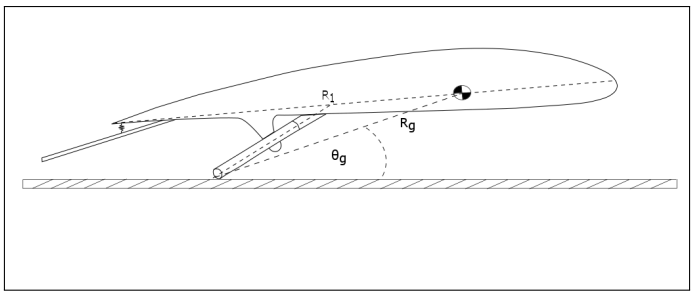

Figure 4.0.2: Rendering of the punting phase

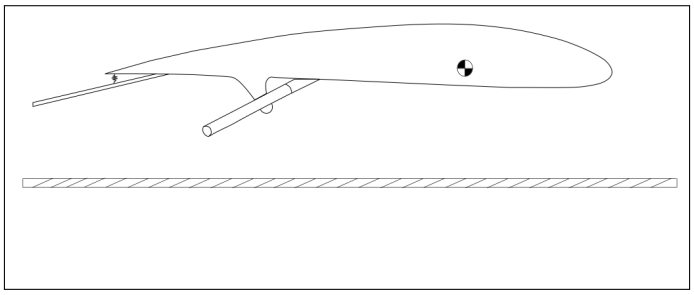

Figure 4.0.3: Rendering of the glide phase

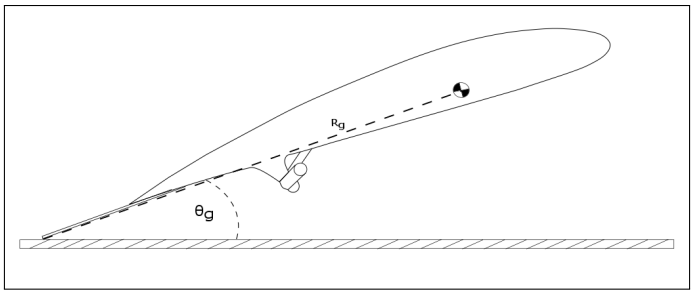

Figure 4.0.4: Rendering of the tail contact phase

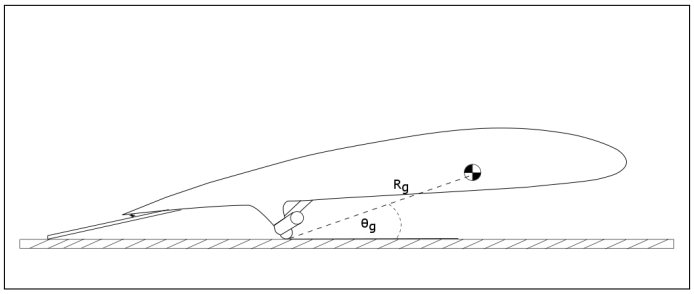

Figure 4.0.5: Rendering of the mount contact phase

4.1 Glide Phase

A simplified 2-dimensional model was developed in order to provide insight into the vehicle dynamics during the glide phase of the 'punting' motion as well as to provide a theoretical reference for the results obtained through experiment.

4.2 Kinematics

The general equations of motion for the vehicle in 2 dimensions are as follows[Fossen, 1994].

$$X = m[\dot{u} + qw - rv + \dot{q}z_g - (r)y_g + (qy_g + r\dot{z_g})p - (q^2 + r^2)x_g] \tag{1}$$

$$Y = m[\dot{v} + ru - pw + \dot{r}x_g - \dot{p}z_g + (rz_g + px_g)q - (r^2 + p^2)y_g] \tag{2}$$

$$\begin{aligned} N = {} & I_{zz}\dot{r} + (I_{yy} - I_{xx})qp + I_{zz}\dot{p} + I_{zy}\dot{q} + I_{xy}(p^2 - q^2) + I_{zy}rp - I_{zx}rq \\ & + m[x_g(\dot{v} + ru - pw) - y_g(\dot{u} + qu - rv)] \end{aligned} \tag{3}$$

Where u is surge, v is heave, w is sway, p is roll, q is sway, and r is pitch. The distance from the origin to the vehicle's center of gravity are x_g, y_g, and z_g.

4.3 Assumptions and Simplified Equations

1. Initial conditions at start of glide phase are known. Include:
   (a) Vertical, horizontal and rotational positions.
   (b) Vertical, horizontal and rotational velocities.
   (c) Vertical, horizontal and rotational accelerations.
2. Equation of Motion Simplifications in Body Fixed Reference Frame
   (a) No sway: $w = 0, \dot{w} = 0$
   (b) No roll: $p = 0, \dot{p} = 0$
   (c) No yaw: $q = 0, \dot{q} = 0$
   (d) The origin is at the center of gravity: $x_g = 0, y_g = 0, z_g = 0$
3. The tail has no effect during the glide phase.

4. The vehicle can be treated as an ellipsoid of similar dimensions

After applying assumptions items 2a to 2d, eqs. (1) to (3) simplify to

$$X = (m_{veh} + m_{11})[\dot{u} - rv] \tag{4}$$

$$Y = (m_{veh} + m_{22})[\dot{v} + ru] \tag{5}$$

$$N = (I_{zz} + m_{66})\frac{dr}{dt} \tag{6}$$

4.4 Added Mass

To find an approximate added mass of the vehicle, assumption 4 allows us to calculate it as an ellipsoid as shown in Figure 4.4.1. with $R_1 = .35m, R_2 = .07m$, and $R_3 = .305m$.

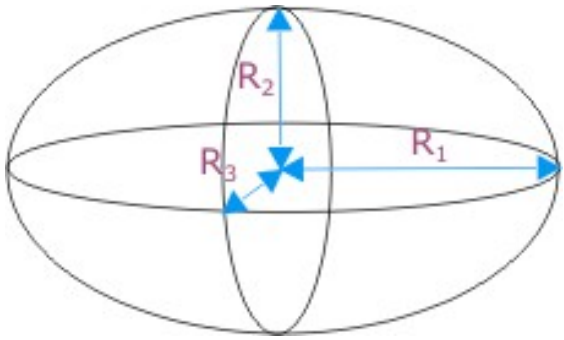

Figure 4.4.1: An ellipsoid

Added mass coefficients for 3 dimensional bodies can be calculated by using strip theory which integrates the added mass coefficients of the cross sections along one axis to give an approximate coefficient for the entire body.[Newman, 1977] Integrating along R_1 gives a cross section in the shape of an ellipse with radii R_2 and R_3. The added mass coefficients for an ellipse are shown in Figure 4.4.2 with m_{11} being a force in the horizontal direction due to a unit acceleration in the

horizontal direction, m_{22} is a vertical force due to vertical acceleration and m_{66} being a moment due to unit rotational acceleration about the origin.

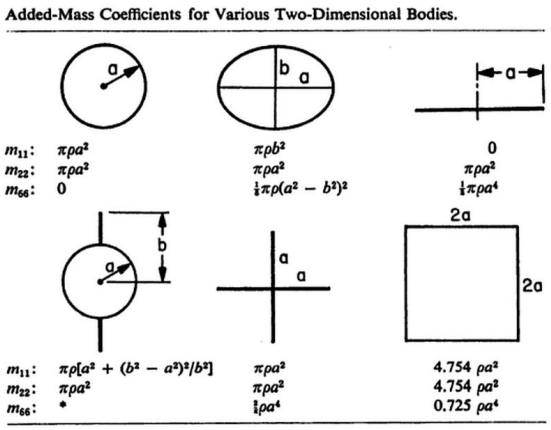

Figure 4.4.2: Added Mass Coefficients for Simple Geometries [Newman, 1977]

The added masses for the vehicle were calculated with the integrals shown in eqs. (7) to (9)

$$m_{11} = \rho\pi \int_{-R_3}^{R_3} (1 - \frac{x^2}{R_3}) R_1 dx \tag{7}$$

$$m_{22} = \rho\pi \int_{-R_1}^{R_1} (1 - \frac{x^2}{R_1}) R_3 dx \tag{8}$$

$$m_{66} = \rho\pi \int_{-R_1}^{R_1} x^2 (1 - \frac{x^2}{R_1}) R_3 dx \tag{9}$$

where ρ is the density of water.

4.5 Moment of Inertia

The rotational moment of inertia, I_{zz} of the vehicle about its center of gravity was obtained from a 3 dimensional model of the vehicle body created in Solidworks, Figure 4.5.1.

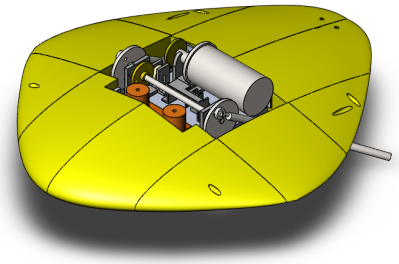

Figure 4.5.1: Model used for Calculation of Rotational Moment of Inertia

4.6 Forces

4.6.1 Buoyant Force

$$F_b = V_{veh}\rho g \tag{10}$$

$$M_b = F_b * d_b \tag{11}$$

where the volume of the vehicle, V_{veh} and center of buoyancy were obtained from a Solidworks model, d_b is distance between the center of gravity and the center of buoyancy and g is the acceleration due to gravity.

4.6.2 Force of Gravity

$$F_g = m_{veh}g \tag{12}$$

4.6.3 Lift and Drag

Due to the irregular shape of the vehicle and the dynamic motion of the vehicle, modeling of the vehicle as a static foil failed. Instead the fluid force were modeled as only drag on a body. Vertical and horizontal drag coefficients were found using flow simulations on the solidworks model. Figure 4.6.1 shows the pressure field on the vehicle at 6 degree angle of attack. The pressure field shows

that the flow around the vehicle does not parallel that of a foil. For this reason instead of lift and drag being calculated it was decided to determine a vertical and horizontal drag coefficient for the vehicle using equation 13. Figures 4.6.4, 4.6.3 and 4.6.2 show the pressure fields from the calculations of force on the body for flows horizontal, and vertical to the vehicle. Due to the asymmetry of the vehicle, a vertical drag coefficient and center of pressure was found for a flow upwards and a flow downwards. These drag coefficients were used to calculate the vertical and horizontal drag force on the body proportional to the body referenced vertical and horizontal velocities for each time step.

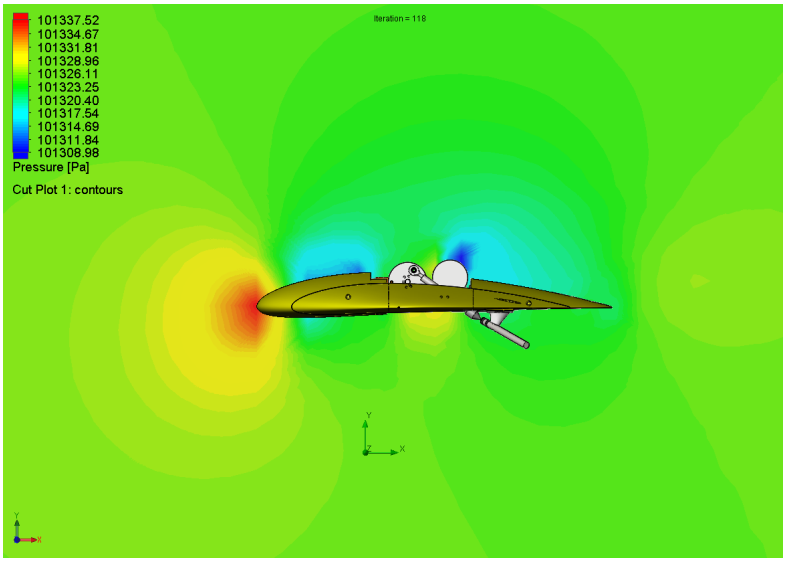

Figure 4.6.1: Pressure field when the vehicle is in a uniform flow with a six degree angle of attack

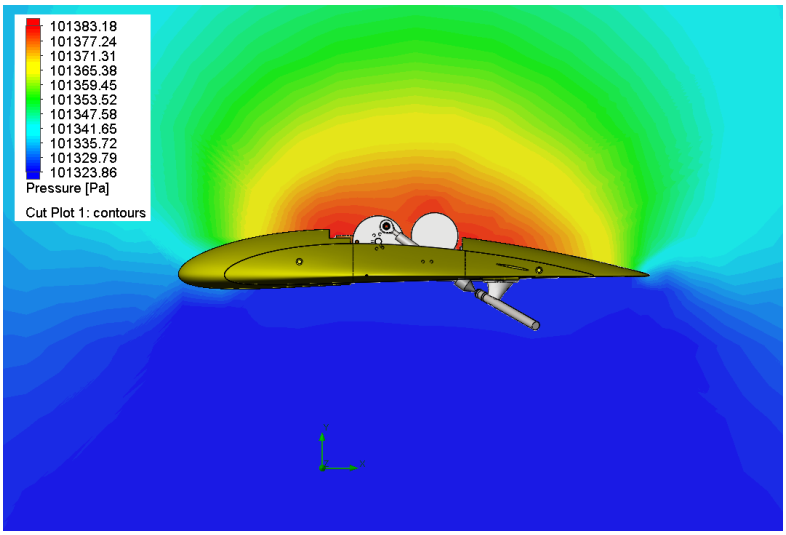

Figure 4.6.2: Pressure on the body when the vehicle moves upwards causing drag

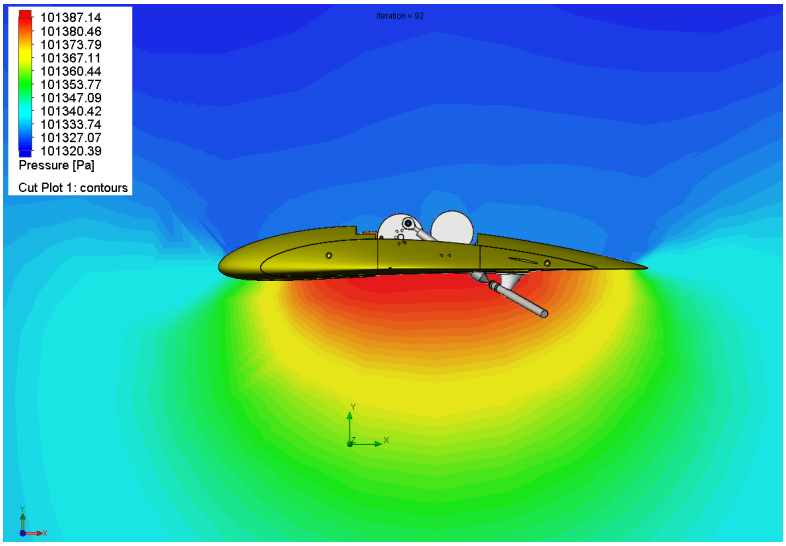

Figure 4.6.3: Pressure on the body when the vehicle moves downwards

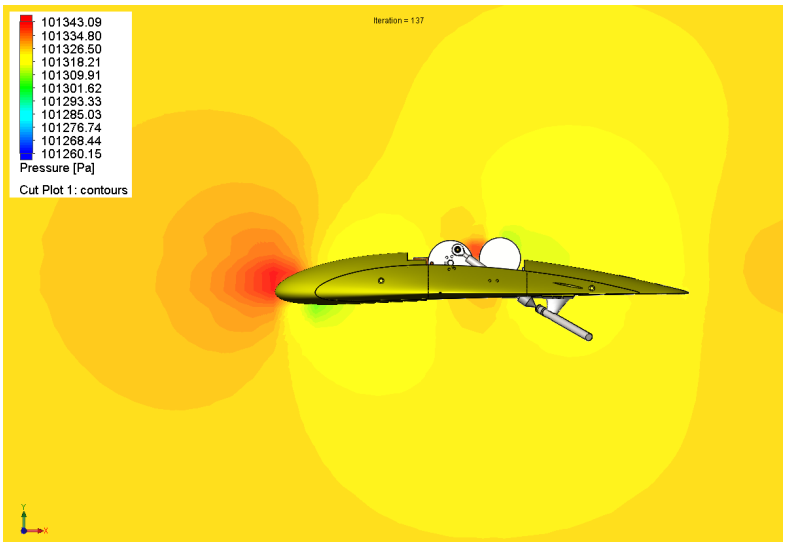

Figure 4.6.4: Pressure field when the vehicle is in a uniform flow with zero angle of attack

$$C_D = \frac{F_D}{\frac{1}{2}\rho A v^2} \tag{13}$$

4.6.4 Munk Moment

The Munk moment is a moment imparted on slender bodies when the body travels at an angle of attack to the flow [Newman, 1977]. The moment tends to drive the body broadside to the flow with a magnitude described in equation eq. (14).

$$M_{munk} = -uv(m_{22} - m_{11}) \tag{14}$$

4.7 Force Balances

The forces are added to the kinematic equations, eqs. (1) to (3), to yield eqs. (15) to (17).

$$X = -F_{drag,horiz} = [m_{veh} + m_{22}][\dot{u} - rv] \tag{15}$$

$$Y = F_{drag,vert} + F_b - F_g + F_{lift} = [m_{veh} + m_{22}][\dot{v} + ru] \tag{16}$$

$$N = -F_{lift} d_{lift} \cos(\theta) - F_b d_b \cos(\theta) + M_{munk} = [I_{zz} + m_{66}] \frac{dr}{dt} \tag{17}$$

4.8 Iterative Calculations

Using the simplified equations of motions, defined coefficients and specified forces, the motion of the vehicle was modeled in steps with a time increment of .01 seconds.

1. Body Referenced Accelerations

$$\dot{u}(t + \delta t) = \frac{F_{drag,horz} + [m_{veh} + m_{22}] r(t) v(t)}{[m_{veh} + m_{22}]} \tag{18}$$

$$\dot{v}(t + \delta t) = \frac{F_{drag,vert} + F_g + F_b + F_{lift} - [m_{veh} + m_{22}] r v(t)}{m_{veh} + m_{22}} \tag{19}$$

$$\dot{r}(t + \delta t) = \frac{-F_b d_b |\cos(\theta(t))|}{I_{zz} + m_{66}} \tag{20}$$

2. Body Relative Velocities

$$u(t + \delta t) = u(t) + \dot{u}(t + \delta t) * \delta t \tag{21}$$

$$v(t + \delta t) = v(t) + (\dot{v})(t + \delta t) * \delta t \tag{22}$$

$$r(t + \delta t) = r(t) + \dot{r}(t + \delta t) * \delta t \tag{23}$$

3. Position

$$x(t + \delta t) = x(t) + Vx(t + \delta t) * \delta t \tag{24}$$

$$y(t+\delta t) = y(t) + Vy(t+\delta t) * \delta t \tag{25}$$

$$\theta(t+\delta t) = \theta(t) + r(t+\delta t) * \delta t \tag{26}$$

4. Inertial Frame Velocities

$$Vx(t) = \cos(\theta)u(t) + \sin(\theta)v(t) \tag{27}$$

$$Vy(t) = -\sin(\theta)u(t) + \cos(\theta)v(t) \tag{28}$$

The results were plotted as followed and compared to the trial data extracted from video.

4.9 Results and Discussion

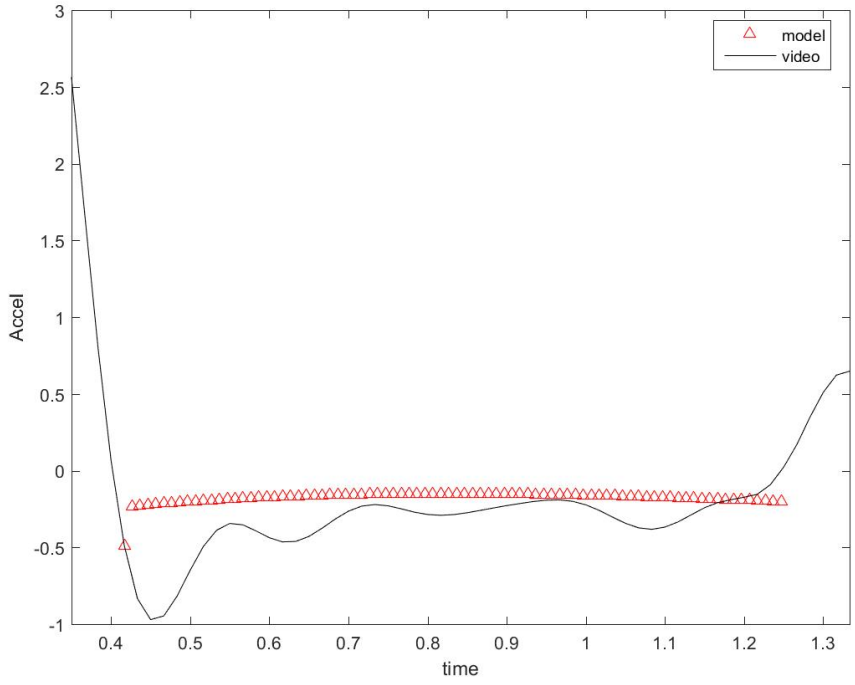

Figure 4.9.1: Horizontal Acceleration comparison between video capture and modeled for a delay of 1000ms

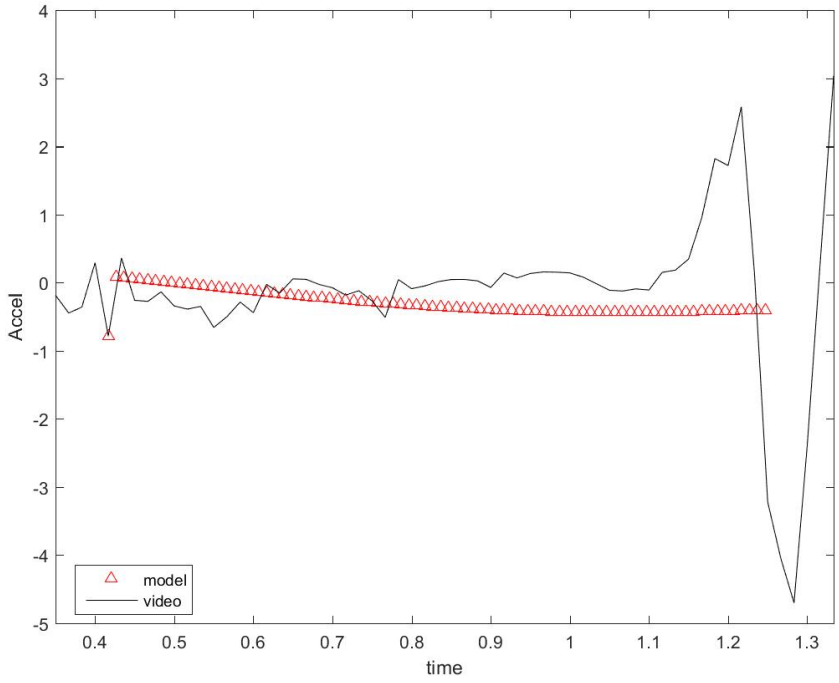

Figure 4.9.2: Vertical Acceleration comparison between video capture and modeled for a delay of 1000ms

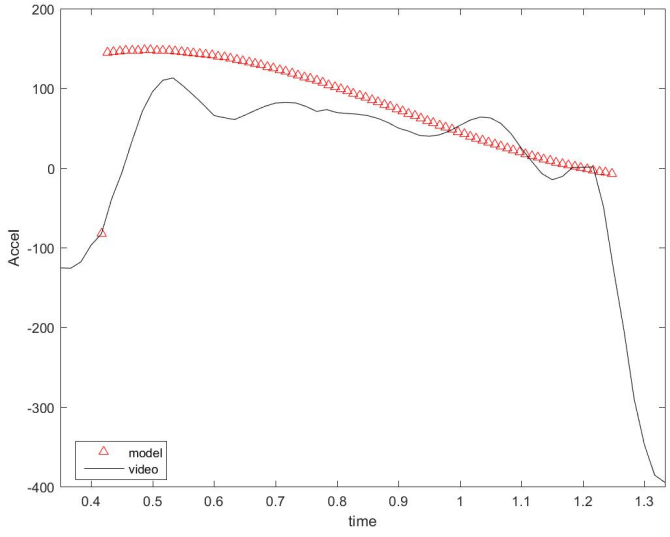

Figure 4.9.3: Radial Acceleration comparison between video capture and modeled for a delay of 1000ms

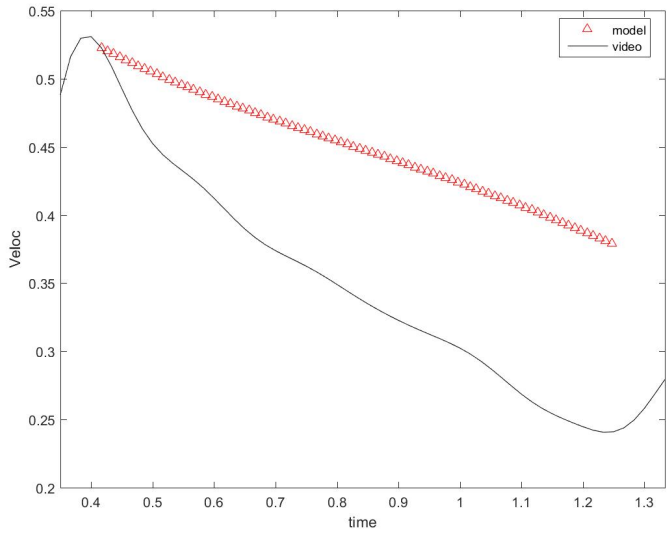

Figure 4.9.4: Horizontal Velocity comparison between video capture and modeled for a delay of 1000ms

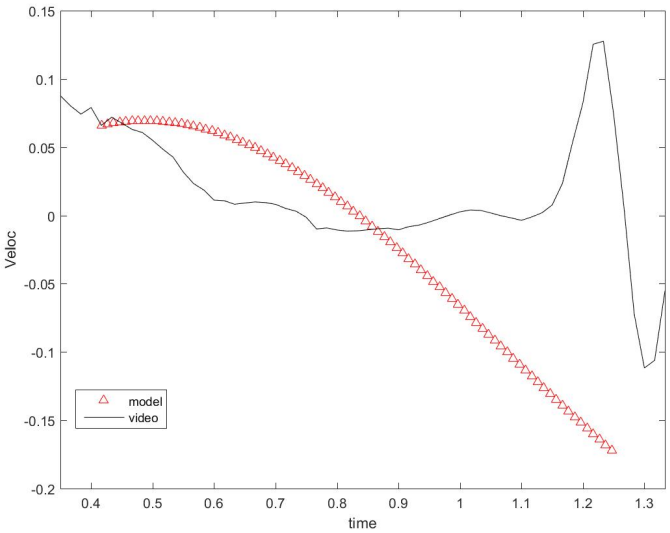

Figure 4.9.5: Vertical Velocity comparison between video capture and modeled for a delay of 1000ms

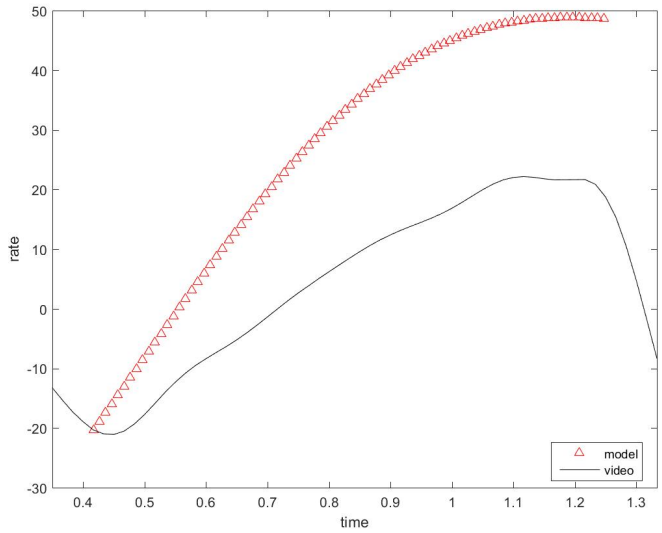

Figure 4.9.6: Radial Velocity comparison between video capture and modeled for a delay of 1000ms

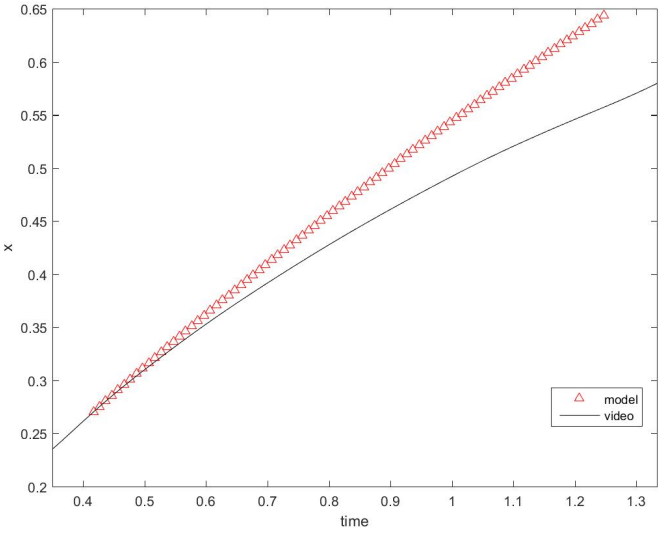

Figure 4.9.7: Horizontal Position comparison between video capture and modeled for a delay of 1000ms

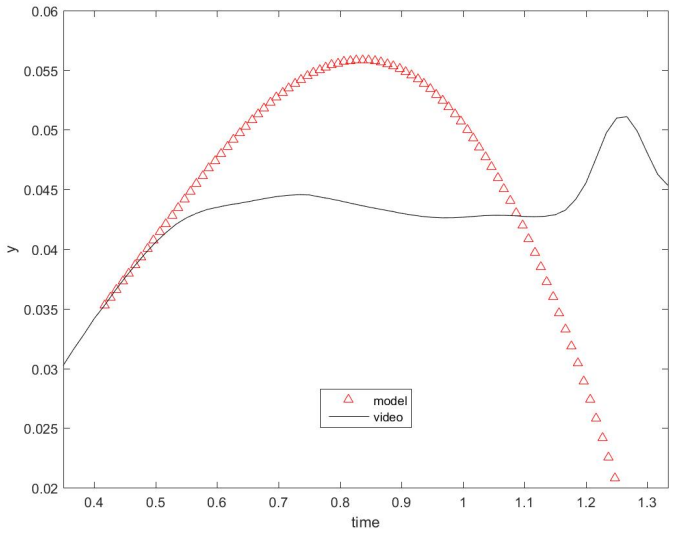

Figure 4.9.8: Vertical Position comparison between video capture and modeled for a delay of 1000ms

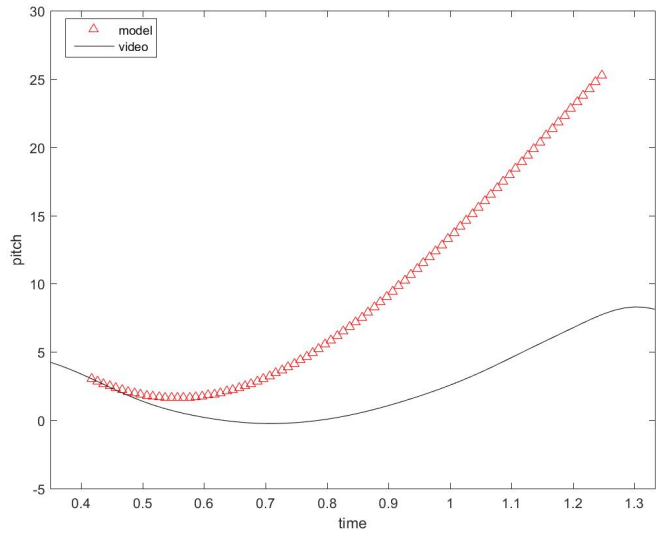

Figure 4.9.9: Radial Position comparison between video capture and modeled for a delay of 1000ms

The results from the modeling compared to the data extracted from the trial videos are shown in figs. 4.9.1 to 4.9.9. The model is able to predict the general trends captured in the video, however, the magnitudes of the accelerations do not

match, and the error in acceleration propagates through to the other modeled values. Throughout the process of modeling the vehicle, the forces were estimated in multiple different ways but varied little between methods. The coefficients of added mass for the vehicle affected the greatest change in accuracy in the modeling, better calculations or measurements of these coefficients would greatly improve the modeling of the vehicle.

CHAPTER 5

Sources of Error and Future Work

There are several sources of error that affect the results shown in the paper. Error in the modeling is likely caused by the irregular shape of the vehicle and the lack of an accurate method estimate the lift, drag and added mass forces on the vehicle. The data collected from the video could also be inaccurate due to motion into or out of the frame that cannot be captured by one camera alone. The current prototype can be used for investigation into varying morphologies and gaits to maximize speed and minimize transport cost. The prototype was designed with large amounts of variability that allow for a wide range of possible experiments. Further investigation can also be performed to determine the effect due to a change in ballast as well as the relation between the center of gravity and the force vector applied to the vehicle by the legs while punting. More research with additional sensors can also move the vehicle from open-loop control to a feedback loop control system.

CHAPTER 6

Conclusions

This thesis details the development and preliminary dynamic trials of a punting underwater vehicle along with preliminary modeling of motion of the vehicle. In-water trials showed that the motion capture algorithm can accurately measure vehicle position and velocity which can be used to validate hydrodynamic models. The development has also provided insight and experience that will be used in the design of future punting vehicles. The trials also identified an optimal pause between kick cycles to maximize speed over ground, however at this point in time it does not lead to a steady state condition across successive kicks. Open loop control was chosen for simplicity in the design of the prototype and also to observe the passive stability of the vehicle. The results show that the vehicle will require feedback in both pitch and altitude to provide adequate control of a punting vehicle. A practical method for modeling of the vehicle is presented and based on the current results, further refinement is needed to accurately predict the motion of the vehicle. The vehicle can be optimized to lessen the extreme changes in pitch and increase glide time to improve performance. From the insight gained with this prototype, future vehicles can be designed to be more easily modeled. Finally, the vehicle has proven that punting is a feasible method of propulsion for undersea vehicles and the platform provides multiple avenues for future work.

Bibliography

Aqua2 autonomous underwater vehicle. http://www.mobilerobots.com/ResearchRobots/aqua2.aspx. Accessed: 2016-02-23.

J. M. Anderson and N. K. Chhabra. Maneuvering and stability performance of a robotic tuna. Integrative and Comparative Biology, 42(1):118–126, 2002. doi: 10.1093/icb/42.1.118.

J. Ayers. Underwater walking. Arthropod Structure & Development, 33(3):347–360, July 2004. ISSN 14678039. doi: 10.1016/j.asd.2004.06.001. URL http://linkinghub.elsevier.com/retrieve/pii/S1467803904000362.

H. Bigelow and W. Schroeder. Fishes of the gulf of maine. Fishery Bulletin of the Fish and Wildlife Service, 53:60–60, 1953.

F. E. Fish, H. Haj-Hariri, A. J. Smits, H. Bart-Smith, and T. Iwasaki. Biomimetic swimmer inspired by the manta ray. In Biomimetics, Biomimetics Series, pages 495–523. CRC Press, 2011. ISBN 978-1-4398-3476-3. URL http://dx.doi.org/10.1201/b11230-18.

T. I. Fossen. Guidance and control of ocean vehicles. John Wiley & Sons Inc, 1994.

C. Georgiades, A. German, A. Hogue, H. Liu, C. Prahacs, A. Ripsman, R. Sim, L.-A. Torres, P. Zhang, M. Buehler, et al. Aqua: an aquatic walking robot. In Intelligent Robots and Systems, 2004.(IROS 2004). Proceedings. 2004 IEEE/RSJ International Conference on, volume 4, pages 3525–3531. IEEE, 2004.

D. M. Koester and C. P. Spirito. Punting: An unusual mode of locomotion in the little skate, leucoraja erinacea (chondrichthyes: Rajidae). Copeia, 2003(3): 553–561, 2003. doi: 10.1643/CG-02-153R1.

S. C. Licht. Biomimetic oscillating foil propulsion to enhance underwater vehicle agility and maneuverability, 2008.

M. Listak, D. Pugal, and M. Kruusmaa. Biomimetic fish-like underwater robot for shallow water applications. In Proc. of the International Conference on Advanced Robotics ICAR, 2007.

L. J. Macesic and S. M. Kajiura. Comparative punting kinematics and pelvic fin musculature of benthic batoids. Journal of Morphology J. Morphol., 271(10): 12191228, Sep 2010. doi: 10.1002/jmor.10865.

N. Mazouchova, P. B. Umbanhowar, and D. I. Goldman. Flipper-driven terrestrial locomotion of a sea turtle-inspired robot. Bioinspiration and Biomimetics, 8(2): 026007, 2013. doi: 10.1088/1748-3182/8/2/026007.

Moog. Miniature High-Torque, Dc Servomotors and DC Gearmotors Technical Data Sheet. URL `http://www.moog.com/literature/MCG/moc13series.pdf`.

J. N. Newman. Marine hydrodynamics. MIT press, 1977.

A. Punning, M. Anton, M. Kruusmaa, and A. Aabloo. A biologically inspired ray-like underwater robot with electroactive polymer pectoral fins. International IEEE Conference on Mechatronics and Robotics, 2004:241–245, 2004.

M. Sfakiotakis, D. M. Lane, and J. B. C. Davies. Review of fish swimming modes for aquatic locomotion. IEEE Journal of Oceanic Engineering, 24(2):237–252, Apr 1999. ISSN 0364-9059. doi: 10.1109/48.757275.

M. Sfakiotakis, A. Kazakidi, and D. P. Tsakiris. Octopus-inspired multi-arm robotic swimming. Bioinspir. Biomim. Bioinspiration and Biomimetics, 10(3): 035005, 2015. doi: 10.1088/1748-3190/10/3/035005.

J. Si and C. Chin. An adaptable walking-skid for seabed ROV under strong current disturbance. Journal of Marine Science and Application, 13(3):305–314, Sept. 2014. ISSN 1671-9433, 1993-5048. doi: 10.1007/s11804-014-1261-y. URL http://link.springer.com/10.1007/s11804-014-1261-y.

K. L. Smith, R. C. Glatts, R. J. Baldwin, S. E. Beaulieu, A. H. Uhlman, R. C. Horn, and C. E. Reimers. An autonomous. bottom-transecting vehicle for making long time-series measurements of sediment community oxygen consumption to abyssal depths. Limnology and Oceanography, 42(7):1601–1612, 1997. URL http://onlinelibrary.wiley.com/doi/10.4319/lo.1997.42.7.1601/full.

J. L. Tangorra, S. N. Davidson, P. G. Madden, G. V. Lauder, and I. W. Hunter. A biorobotic pectoral fin for autonomous undersea vehicles. In Engineering in Medicine and Biology Society, 2006. EMBS '06. 28th Annual International Conference of the IEEE, pages 2726–2729, Aug 2006. doi: 10.1109/IEMBS.2006.260834.

A. H. Techet. Propulsive performance of biologically inspired flapping foils at high reynolds numbers. Journal of Experimental Biology, 211(2):274–279, 2007. ISSN 0022-0949. doi: 10.1242/jeb.012849. URL http://jeb.biologists.org/content/211/2/274.

S. Wood, W. Harris, T. Ismail, J.-M. Malone, M. Nanney, J. Ojeda, B. Pugatch, and S. Vandedrinck. Hybrid robot crawler/flyer for use in underwater archaeology. In Oceans-San Diego, 2013, pages 1–11. IEEE, 2013.

S. L. Wood. Modular amphibious research crawler. Sea Technology, 47(2):71, 2006. URL https://pdfs.semanticscholar.org/1fa9/11ce23faccea9a4554a98654845993c2d7f1.pdf.

S. Zhang, Y. Zhou, M. Xu, X. Liang, J. Liu, and J. Yang. AmphiHex-I: Locomotory Performance in Amphibious Environments With Specially Designed Transformable Flipper Legs. IEEE/ASME Transactions on Mechatronics, 21 (3):1720–1731, June 2016. ISSN 1083-4435, 1941-014X. doi: 10.1109/TMECH.2015.2490074. URL http://ieeexplore.ieee.org/document/7296639/.

Bibliography

Aqua2 autonomous underwater vehicle. http://www.mobilerobots.com/ResearchRobots/aqua2.aspx. Accessed: 2016-02-23.

J. M. Anderson and N. K. Chhabra. Maneuvering and stability performance of a robotic tuna. Integrative and Comparative Biology, 42(1):118–126, 2002. doi: 10.1093/icb/42.1.118.

J. Ayers. Underwater walking. Arthropod Structure & Development, 33(3):347–360, July 2004. ISSN 14678039. doi: 10.1016/j.asd.2004.06.001. URL http://linkinghub.elsevier.com/retrieve/pii/S1467803904000362.

H. Bigelow and W. Schroeder. Fishes of the gulf of maine. Fishery Bulletin of the Fish and Wildlife Service, 53:60–60, 1953.

F. E. Fish, H. Haj-Hariri, A. J. Smits, H. Bart-Smith, and T. Iwasaki. Biomimetic swimmer inspired by the manta ray. In Biomimetics, Biomimetics Series, pages 495–523. CRC Press, 2011. ISBN 978-1-4398-3476-3. URL http://dx.doi.org/10.1201/b11230-18.

T. I. Fossen. Guidance and control of ocean vehicles. John Wiley & Sons Inc, 1994.

C. Georgiades, A. German, A. Hogue, H. Liu, C. Prahacs, A. Ripsman, R. Sim, L.-A. Torres, P. Zhang, M. Buehler, et al. Aqua: an aquatic walking robot. In Intelligent Robots and Systems, 2004.(IROS 2004). Proceedings. 2004 IEEE/RSJ International Conference on, volume 4, pages 3525–3531. IEEE, 2004.

D. M. Koester and C. P. Spirito. Punting: An unusual mode of locomotion in the little skate, leucoraja erinacea (chondrichthyes: Rajidae). Copeia, 2003(3): 553–561, 2003. doi: 10.1643/CG-02-153R1.

S. C. Licht. Biomimetic oscillating foil propulsion to enhance underwater vehicle agility and maneuverability, 2008.

M. Listak, D. Pugal, and M. Kruusmaa. Biomimetic fish-like underwater robot for shallow water applications. In Proc. of the International Conference on Advanced Robotics ICAR, 2007.

L. J. Macesic and S. M. Kajiura. Comparative punting kinematics and pelvic fin musculature of benthic batoids. Journal of Morphology J. Morphol., 271(10): 12191228, Sep 2010. doi: 10.1002/jmor.10865.

N. Mazouchova, P. B. Umbanhowar, and D. I. Goldman. Flipper-driven terrestrial locomotion of a sea turtle-inspired robot. Bioinspiration and Biomimetics, 8(2): 026007, 2013. doi: 10.1088/1748-3182/8/2/026007.

Moog. Miniature High-Torque, Dc Servomotors and DC Gearmotors Technical Data Sheet. URL `http://www.moog.com/literature/MCG/moc13series.pdf`.

J. N. Newman. Marine hydrodynamics. MIT press, 1977.

A. Punning, M. Anton, M. Kruusmaa, and A. Aabloo. A biologically inspired ray-like underwater robot with electroactive polymer pectoral fins. International IEEE Conference on Mechatronics and Robotics, 2004:241–245, 2004.

M. Sfakiotakis, D. M. Lane, and J. B. C. Davies. Review of fish swimming modes for aquatic locomotion. IEEE Journal of Oceanic Engineering, 24(2):237–252, Apr 1999. ISSN 0364-9059. doi: 10.1109/48.757275.

M. Sfakiotakis, A. Kazakidi, and D. P. Tsakiris. Octopus-inspired multi-arm robotic swimming. Bioinspir. Biomim. Bioinspiration and Biomimetics, 10(3): 035005, 2015. doi: 10.1088/1748-3190/10/3/035005.

J. Si and C. Chin. An adaptable walking-skid for seabed ROV under strong current disturbance. Journal of Marine Science and Application, 13(3):305–314, Sept. 2014. ISSN 1671-9433, 1993-5048. doi: 10.1007/s11804-014-1261-y. URL http://link.springer.com/10.1007/s11804-014-1261-y.

K. L. Smith, R. C. Glatts, R. J. Baldwin, S. E. Beaulieu, A. H. Uhlman, R. C. Horn, and C. E. Reimers. An autonomous. bottom-transecting vehicle for making long time-series measurements of sediment community oxygen consumption to abyssal depths. Limnology and Oceanography, 42(7):1601–1612, 1997. URL http://onlinelibrary.wiley.com/doi/10.4319/lo.1997.42.7.1601/full.

J. L. Tangorra, S. N. Davidson, P. G. Madden, G. V. Lauder, and I. W. Hunter. A biorobotic pectoral fin for autonomous undersea vehicles. In Engineering in Medicine and Biology Society, 2006. EMBS '06. 28th Annual International Conference of the IEEE, pages 2726–2729, Aug 2006. doi: 10.1109/IEMBS.2006.260834.

A. H. Techet. Propulsive performance of biologically inspired flapping foils at high reynolds numbers. Journal of Experimental Biology, 211(2):274–279, 2007. ISSN 0022-0949. doi: 10.1242/jeb.012849. URL http://jeb.biologists.org/content/211/2/274.

S. Wood, W. Harris, T. Ismail, J.-M. Malone, M. Nanney, J. Ojeda, B. Pugatch, and S. Vandedrinck. Hybrid robot crawler/flyer for use in underwater archaeology. In Oceans-San Diego, 2013, pages 1–11. IEEE, 2013.

S. L. Wood. Modular amphibious research crawler. Sea Technology, 47(2):71, 2006. URL https://pdfs.semanticscholar.org/1fa9/11ce23faccea9a4554a98654845993c2d7f1.pdf.

S. Zhang, Y. Zhou, M. Xu, X. Liang, J. Liu, and J. Yang. AmphiHex-I: Locomotory Performance in Amphibious Environments With Specially Designed Transformable Flipper Legs. IEEE/ASME Transactions on Mechatronics, 21 (3):1720–1731, June 2016. ISSN 1083-4435, 1941-014X. doi: 10.1109/TMECH.2015.2490074. URL http://ieeexplore.ieee.org/document/7296639/.